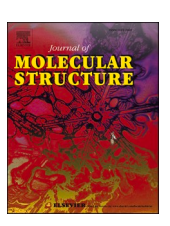
ELSEVIER

Contents lists available at ScienceDirect

# Journal of Molecular Structure

journal homepage: www.elsevier.com/locate/molstr





# Structural investigation and computational insight of binary molecular salt crystals of gallic acid with 2-aminopyridine and 3-aminopyridine

K.L. Jyothi <sup>a,\*</sup> , Karthik Kumara <sup>b,c</sup> , Viswanath M. Arya <sup>b</sup>, Vallabh S. Ghantasala <sup>d</sup>, T.N. Guru Row <sup>e</sup>, N.K. Lokanath <sup>f,\*</sup>

- <sup>a</sup> Department of Physics, Government First Grade College, Bengaluru North University, Sidlaghatta, 562105, India
- <sup>b</sup> Department of Physics, B.M.S. College of Engineering, Bengaluru, 560019, India
- <sup>c</sup> BSN Centre for Nano-Materials and Displays, B.M.S. College of Engineering, Bengaluru, 560019, India
- <sup>d</sup> School of Computer Science and Engineering (SCOPE), VIT-AP University, Amaravati, 522237, India
- <sup>e</sup> Solid State and Structural Chemistry Unit, Indian Institute of Science, Bengaluru, 560012, India
- f Department of Studies in Physics, University of Mysore, Manasagangotri, Mysuru, 570006, India

#### ARTICLE INFO

# Key words: Multicomponent crystal forms API Molecular salts DFT Hirshfeld surface analysis Molecular docking

#### ABSTRACT

The performance parameters of active pharmaceutical ingredients (APIs) can be tuned to desired values by obtaining their multicomponent forms using suitable coformers and the pharmaceutical applications of these multicomponent forms are decided through the structural studies. With the objective to contribute novel crystal forms of the gallic acid (API), in this article we are reporting the preparation and structural studies using single crystal X-ray diffraction of two molecular salt binary crystals of gallic acid (GA) with 2-aminopyridine (2AP) and 3-aminopyridine (3AP). Confirmation of the interactions between API and coformers was made through PXRD, FTIR, and UV-Vis experimental techniques. Among the two, GA-2AP was crystallized in 2:2 stochiometric ratio whereas, GA-3AP was crystallized in 1:1 stochiometric ratio. Expected  $R_2^2(8)$  and  $R_1^2(5)$  ring motifs occurred between acid and pyrimidine bases. The thermal behaviour and hence stability of the two compounds were evaluated by the TGA and DTA experiments. Inter molecular interactions of the compounds were investigated using the 3D Hirshfeld surfaces and the associated 2D fingerprint plots. To assess the degree to which chemical entities interact in a crystalline environment, enrichment ratio calculations was performed. Through DFT study, the chemical and physical reactive parameters were determined. The molecular docking study of the two molecular salts was carried out against 6LU7 (A), 6VSB (B), and 6VYB (C) targets of Covid-19 virus.

#### 1. Introduction

Understanding the nature of crystal packing and its influence upon the physicochemical properties of various crystal forms of active pharmaceutical ingredient (API) is the fundamental requirement of the pharmaceutical industries [1–5]. This is because, the integral part of drug development process encompasses, screening and identification of an optimal crystal form to afford a high purity product with reliable reproducibility and scalability [6–9]. As these crystal forms are thermodynamically more stable when compared to amorphous solids, drug developers and regulatory bodies prefer these crystal forms [10–12]. Based on the solubility and permeability, Biopharmaceutical Classification Scheme (BCS) has categorized the drug substances into four classes [13]. Class I: high solubility, high permeability; Class II: low

solubility, high permeability; Class III: high solubility, low permeability; Class IV: low solubility, low permeability. It is useful to the formulation researchers to develop novel dosage forms based on modernistic rather than experimental approaches. Literature shows that majority of APIs fall into BCS class II (low solubility, high permeability). These APIs can be shifted to class I by increasing their solubility. This can be done by obtaining multicomponent crystal forms of APIs [14] namely; salts, cocrystals, solvates, or hydrates, polymorphs and their combination. These crystal forms alter the properties like solubility and hygroscopicity of API, offering enhanced thermodynamic equilibrium compared to unblemished crystalline structures. These crystal forms can be obtained through non-covalent intermolecular interactions (like H-bonding and  $\pi\text{-}\pi$  stacking) between API and coformers (without altering covalent bonding). Designing and development of these multicomponent crystal

E-mail addresses: kljyothishekar@gmail.com (K.L. Jyothi), lokanath@physics.uni-mysore.ac.in (N.K. Lokanath).

<sup>\*</sup> Corresponding authors.

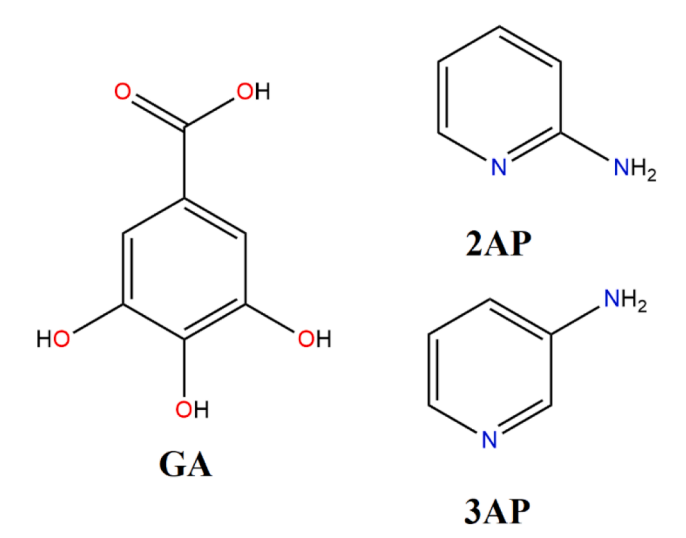


Fig. 1. Schematic diagrams of gallic acid (GA), 2-aminopyridine (2AP), and 3-aminopyridine (3AP).

forms of API is the current major challenge and opportunity to the pharmaceutical industry.

Pharmaceutically important multicomponent crystals can be prepared by suitably selecting API and coformers [15,16] and taking them in particular molar ratio. Literature survey helps in selecting API whereas, coformers can be selected using hydrogen bonding and supramolecular synthon approaches. One can also make use of CSD data base facility for selecting coformers. Among the various available solvent based and solid based preparation methods [17], a particular method suitable for the decided API and coformer/s can be selected. By knowing the position and number of hydrogen bonding sites of API and coformer/s, one can also predict possible intermolecular interactions and supramolecular synthons between them. The stoichiometry of the constituents in the prepared multicomponent compound doesn't only depends on their molar ratio but also on the mode of hydrogen bonding interactions which intern depends on various internal and external factors [18].

The diverse functional groups in drug molecules often exhibits significant challenges in designing and controlling the crystal forms of API. The most common multicomponent crystal forms of APIs are ionized acid-base pairs, or molecular salts. By definition, molecular salt formation involves a proton transfer from the acidic moiety to the basic moiety, forming ionic components of opposite charges. However, many organic basic groups are weak bases and many organic acids are weak acids due to their inherent molecular composition and charge distribution. In addition, more than one basic or acidic group may be present, which naturally creates competition between these functional groups. As a result of competition, cooperation and balance between different intermolecular forces in a multicomponent system, an acid-base pair may not necessarily constitute a molecular salt due to either partial or absent proton transfer. Lack of proton transfer results in a crystalline complex that contains two or more different neutral molecules, and is named a cocrystal. The  $\Delta pKa$  rule can generally be considered as a useful indicator in crystal engineering to predict the formation of cocrystals and molecular salts when acids and bases are taken as starting compounds [19]. According to this rule, the  $\Delta pKa$  value (= pKa(base) - pKa(acid)) is greater than 3 this will lead to the formation of molecular salt. If  $\Delta pKa$  value is less than zero i.e., negative then this leads to the formation of cocrystals. Suppose if  $\Delta pKa$  value lies between 0 and 3, the combination of acid and base can result in the formation of either molecular salt or cocrystals.

As powder X-ray diffraction (PXRD) and Fourier transform infrared (FTIR) spectroscopy patterns are the fingerprints of the substance, these methods are used as preliminary characterization techniques to confirm

the interaction between API and conformer/s and hence the formation of new crystal phases [20,21]. Other characterization techniques like NMR, UV-Vis spectroscopy, Raman spectroscopy, TGA, DTA, DSC will provide structural information of the multicomponent compound [22, 23]. But, the final examination of the compound to elucidate its complete three-dimensional crystal structure, for understanding their structure—property relationships, can be performed using single crystal X-ray diffraction technique [24–26].

While doing literature survey in search of an API having good number of hydrogen bonding sites, a phenolic acid compound, trihydroxy benzoic acid with hydroxyl groups at the 3, 4, and 5 positions of the benzene ring and a carboxyl group known as gallic acid (GA) found interesting [Fig. 1]. Gallic acid is found to be well known for its various therapeutic effects including antibacterial, antiviral, antitubercular, and antifungal [27-32]. By looking at its numerous medicinal values, properties, and applications we selected GA as API for our work. Then from the CSD database we found that pyridine derivative compounds will easily involve in the formation of supramolecular synthon formation with the compounds having carboxyl functional group. Also, pyrimidines and aminopyrimidine derivatives are biologically important compounds and they manifest themselves in nature as components of nucleic acids [33-35]. We selected 2-aminopyridine (2AP) and 3-aminopyridine (3AP) (Fig. 1) as coformers to prepare and study binary compounds with gallic acid. Ramdas et al. [36] have studied 2-aminopyridine molecule and showed that 2AP molecules can be used as pharmacophores against various biological targets. Stephen et al. [37] have reported that the derivatives of 2-aminopyridine shows activity in cell-based mechanistic assays for inhibition of CHK2. Further, Zahira et al. [38] have showed the derivatives of 2AP molecule can be used as an antibacterial agent model with high antibacterial potency. Further, Rick et al. [39] have demonstrated the clinical potential of another coformer i.e., 3AP as an antineoplastic agent. Baranyi et al. [40] have successfully examined the effects of 3AP on pyramidal tract neurones in the motor cortex of anesthetised cat. Jiang et al. [41] reported that the derivatives of 3AP has a high potential for development as a novel, potent neuroprotectant for the treatment of neurodegenerative diseases. The pharmaceutical and biological importance of the gallic acid has driven to exploit its various multicomponent crystal forms and to investigate its rich structural diversity. This offers an opportunity for the pharmaceutical industry to address its new intellectual properties, which expands the drug life of the gallic acid.

In this paper we are reporting preparation, preliminary characterizations and the elucidation of crystal structure of GA-2AP and GA-3AP binary crystals. Further, to provide a comprehensive understanding of their structure, properties, and formation, additionally we carried out computational Hirshfeld surface analysis and DFT study. Furthermore, we are reporting enrichment ratio calculation and molecular docking studies to explore the possible molecular interactions with the targeted Covid-19 viruses.

# 2. Materials and methods

# 2.1. Preparation and crystal growth

About 0.340 grams of gallic acid (GA) is taken with 0.188 grams of 2-aminopyridine (2AP) and with 0.188 grams of 3-aminopyridine (3AP) separately in different mortars to form GA-2AP and GA-3AP mixtures of 1:1 molar ratio. The mixtures are subjected to manual neat grinding using a pestle for about 20 minutes. Further, the mixtures were subjected to liquid-assisted grinding for another 20 minutes by adding a few drops of acetonitrile liquid [42–44]. Then the formation of the binary compounds in new crystal phases in comparison with the pure initial compounds weres confirmed from the PXRD technique and the novelty of the prepared compounds were further confirmed by the FTIR spectroscopic technique. After the confirmations from the preliminary characterizations, to carry out the structural study, the crystals of the mixtures were

obtained using the slow evaporation method. Based on solubility considerations of the initial components of the binary compounds, methanol was chosen as the solvent to enhance the probability of nucleation during crystal growth [45,46]. The supersaturated solution of the 1:1 GA-2AP and 1:1 GA-3AP compounds were prepared with the help of sonication and magnetic stirring. Then the solutions were kept undisturbed for slow and complete evaporation by covering the beakers with parafilm. Block-shaped brown-colored GA-2AP crystals and block-shaped colorless GA-3AP crystals suitable to carry out single-crystal X-ray diffraction experiments were obtained within two weeks.

#### 2.2. Powder X-ray diffraction (PXRD)

Powder X-ray diffraction technique is the most widely used for the identification of crystalline phases of the material which gives the unique powder X-ray diffraction pattern which is considered as the fingerprint of the compound [47]. So, to confirm the interactions between the initial compounds and hence the formation new crystalline phase, PXRD experiments were carried out on a PAN analytical X'Pert diffractometer using Cu-Kα radiation ( $\lambda=1.54056~\mbox{Å}$ ), operated at 30 mA and 40 kV. Diffraction data of initial compounds and the mixtures were collected at room temperature over a 20 range of 0-50° in continuous scan mode with a step size of 0.02°. Powder diffraction patterns were plotted and analyzed using X'Pert HighScore Plus.

#### 2.3. Fourier transform infrared spectroscopy (FTIR)

Fourier transform infrared (FTIR) spectroscopy is a non-destructive chemical characterization technique that encompasses the infrared radiation of the electromagnetic spectrum [48]. The mid-infrared (4000  ${\rm cm}^{-1}$  - 200  ${\rm cm}^{-1}$ ) radiation is called the "fingerprint region" and the FTIR spectrum of the compound obtained in this wavenumber range provides a unique spectral signature of the compound. So, for further confirmation of the formation of the new compound, which results in a change in the stretching (changes in bond length) and bending (changes in the bond angle) vibrations, FTIR characterization is performed. As the combination of acid and base compounds were taken, it may result in the formation of molecular salt due to proton transfer from the carboxylic acid group which results in the formation of a carboxylate anion in the compound. The proton transfer and hence the formation of carboxylate anion (COO-) is confirmed by the absence of absorption bands of functional groups; C = O & C - O and the presence of a characteristic absorption band of asymmetric stretching vibration between 1550 cm<sup>-1</sup> and 1620 cm<sup>-1</sup>. Hence, FTIR analysis was performed using PerkinElmer instrument, in the range 4000 to 400 cm<sup>-1</sup>. A resolution of 4 cm<sup>-1</sup> was used to record the infrared spectra of the powder samples. Absorption peaks of the functional groups were identified; wavenumbers were assigned and are tabulated for the analysis.

# 2.4. UV-Vis spectroscopy

UV spectroscopy stands as a robust analytical technique with wideranging applications, making it a cornerstone in scientific research and analysis [49]. The fundamental principle of UV spectroscopy lies in the absorption of specific wavelengths (of 200nm to 800nm) of light by samples, and it provides valuable informations of the substances. In order know the band gap energy values, UV-Vis absorption experiement was carried out for both initial compounds and binary materials [50]. Solid-state UV visible absorption spectra were recorded in PerkinElmer (Lambda-365+) double beam spectrophotometer using ethanol solvent as reference.

# 2.5. Single crystal X-ray diffraction studies (SCXRD)

Good quality single crystals of the GA-2AP of dimension 0.25  $\,\times$ 

 $0.12 \times 0.10$  mm and GA-3AP with dimension  $0.21 \times 0.20 \times 0.15$  mm were selected using a polarizing microscope. The X-ray intensity data of the title compounds were collected at 296 K on a Bruker Proteum2 CCD diffractometer with X-ray generator operating at 45 kV and 10 mA, using CuKα radiation of wavelength 1.54178 Å. Data were collected for 24 frames per set with different settings of  $\varphi$  (0° and 90°), keeping the scan width of 0.5°, exposure time of 5 s, the sample to detector distance of 45.10 mm. The complete intensity data sets were processed using SAINT PLUS [51] and the absorption correction was conducted with the multi-scan method. The crystal structures were solved by the direct method, and the position of all non-hydrogen atoms was identified and refined on  $F^2$  by a full-matrix least-squares procedure using anisotropic displacement parameters by using SHELXS [52] and SHELXL [53] programs. All the hydrogen atoms were located in difference Fourier maps and treated as riding on their atoms with isotropic thermal displacement parameters. The geometrical calculations were carried out using the crystallographic program PLATON [54]. The crystal packing diagrams were generated by the MERCURY software [55].

#### 2.6. Thermogravimetric analysis (TGA)

Thermogravimetric analysis (TGA) is a powerful technique for the measurement of thermal stability of materials [56]. In this method, changes in the weight of a material are measured by increasing its temperature which helps in knowing the melting point and decomposition point. To study the thermal stability of the two novel (GA-2AP and GA-3AP) crystals, thermogravimetric analysis was carried out by heating the crystals of GA-BU in the Mettler-Toledo TGA/SDTA 851e thermal analyser under a flow of  $\rm N_2$  (40 ml min $^{-1}$ ). The crystals were heated at a rate of  $\rm 10^\circ C~min^{-1}$  from  $\rm 30^\circ C$  to  $\rm 600^\circ C$  with inert alumina as a reference. Thermograms were plotted and analysed.

#### 2.7. Differential thermal analysis (DTA)

Differential Thermal Analysis (DTA) is an analytical technique that measures the temperature difference between a sample and an inert reference material as they are subjected to a controlled heating or cooling program. This temperature difference detects thermal transitions, such as melting, crystallization, decomposition, or oxidation, which involve the absorption or release of heat. The resulting DTA curve, a plot of the heat flow versus temperature or time, provides information about the sample's thermal properties and chemical changes [57,58]. Differential Thermal Analysis (DTA) was employed to investigate the thermal behaviour and phase transition temperatures of the synthesized molecular salt crystals. The analysis was performed on a SHIMADZU DTA-TG-60 instrument. For each measurement, a sample mass of approximately 7.0 mg was heated from ambient temperature to 350°C at a constant rate of 10°C min<sup>-1</sup> under a dynamic oxygen atmosphere (flow rate: 10 mL min<sup>-1</sup>).

# 2.8. Hirshfeld surface analysis

Intermolecular hydrogen bonding interactions and crystal packing properties are closely related. The intermolecular interactions exhibited by the supermolecule in the crystalline environment can be understood from Hirshfeld surface analysis (HSA) [59]. In this method, the molecular Hirshfeld surface is constructed by calculating the electron distribution of the molecule using the sum of the spherical atom electron density. This is performed by loading the crystallographic information file (CIF) to the CrystalExplorer software [60]. The molecular Hirshfeld surface mapped with 3D  $d_{\rm norm}$  and 2D fingerprint plots (FPs) were obtained with the help of  $d_{\rm e}$  and  $d_{\rm i}$  values, and the van der Waal's atomic radii (r) the equation given below, which enables to identify the regions of specific importance related to the intermolecular interactions.

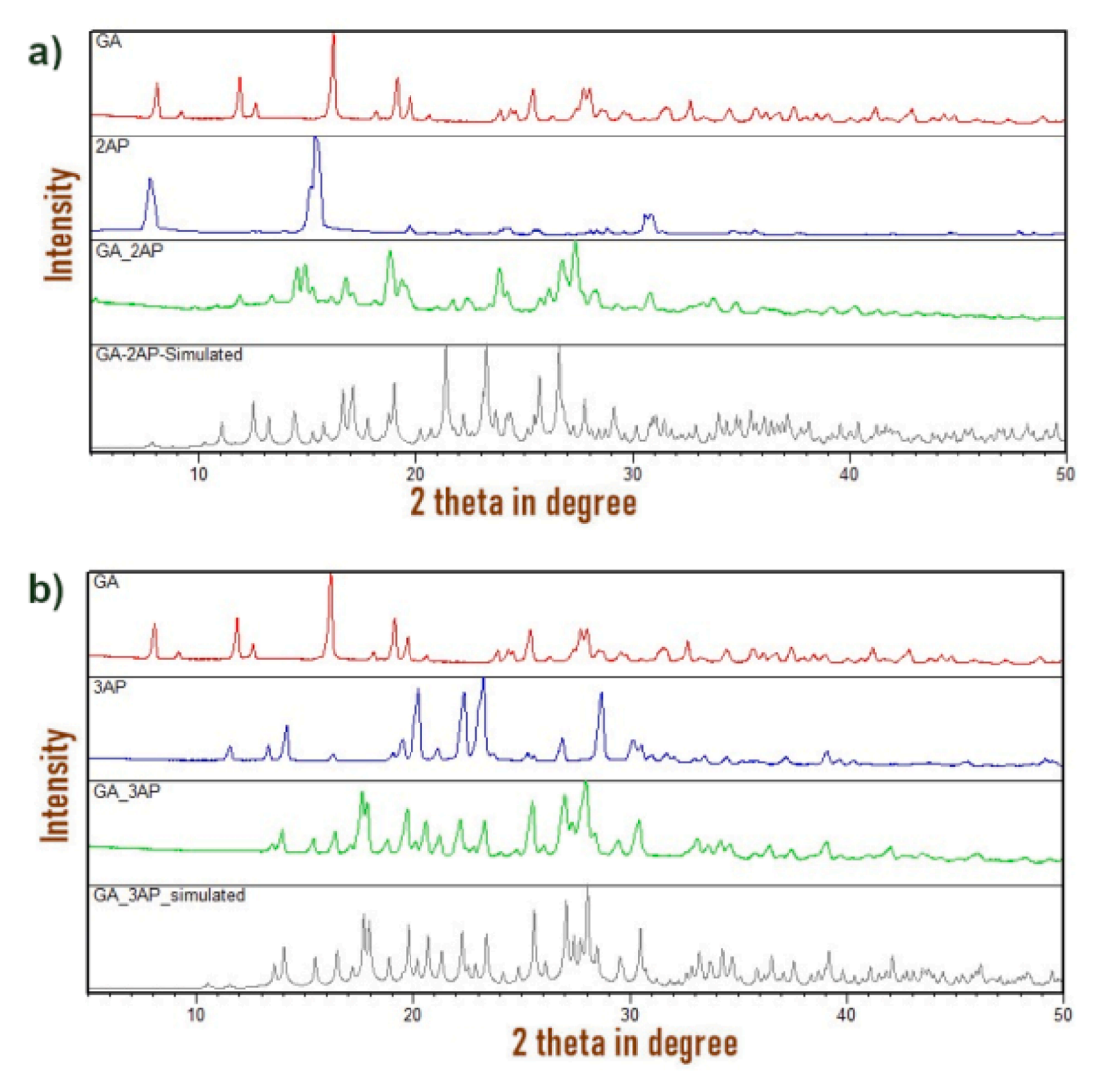


Fig. 2. Powder X-ray diffraction patterns for initial compounds, co-grinding products along with the PXRD pattern simulated from the single-crystal X-ray diffraction analysis of a) GA-2AP molecular salt compound and b) GA-3AP molecular salt compound.

$$d_{norm} = rac{d_i - r_i^{
u dw}}{r_i^{
u dw}} + rac{d_e - r_e^{
u dw}}{r_e^{
u dw}}$$

Here  $d_i$  is the distance from a given point on the Hirshfeld surface to the nearest nucleus inside the surface and  $d_e$  is the distance from a point to the nearest nucleus outside the surface.

The red-blue-white colored spots on the  $d_{\rm norm}$  surface represent different intermolecular interactions. The shorter inter contacts are represented by red-colored regions, longer inter contacts are represented by the blue-colored regions whereas, the contacts around the van der Waal's radii are represented by white-colored regions. The fingerprint plot tells the contribution of each individual intermolecular interaction to the surface and can be understood through color codes (frequency of presence) ranging from blue color (few points) through green color to red color (many points). Further, HSA also helps to understand the stability of the crystal structure through the stacking interactions. The  $d_{\rm i}$ ,  $d_{\rm e}$ , shape index, curvedness surfaces and fragment patch of the Hirshfeld surface generated will give more information about the stacking interactions [61].

# 2.9. Interaction energies and energy frameworks

The molecular interaction energies (such as; electrostatic, polarization, dispersion and exchange-repulsion energies) in the crystalline

environment play an important role in the understanding of crystal packing [62]. Electrostatic energy gives information about the coulombic attraction/repulsion between the molecules, dispersion energy provides information about van der Waals attractions due to correlated fluctuations, polarization energy gives information about dipole-induced interactions, whereas the repulsion energy represents the Pauli exclusion. Hence, the total interaction energy value, which is the sum of electrostatic, polarization, dispersion and exchange-repulsion energies between molecular pairs, is very useful to get information about the thermal stability of the compound. These interaction energies and hence the total interaction energy can be calculated using B3LYP/6-31G(d,p) molecular wavefunctions with the aid of the most effective method using Crystal Explorer 17.5 software. The interaction energies are computed by generating the molecular cluster of radius 3.8 Å around the selected molecule [63].

Further, the graphical representation of these energies known as energy frameworks. These energy frameworks offer a powerful and unique way to visualize the supramolecular architecture of molecular crystal structures and helps in estimating the mechanical properties of the crystals [63]. Energy frameworks are represented as cylinders joining the centres of mass of the molecules, with the cylinder radius proportional to the magnitude of the interaction energy. The cylinders that make up the framework represent the relative strengths of molecular packing in different directions. The interaction energy framework

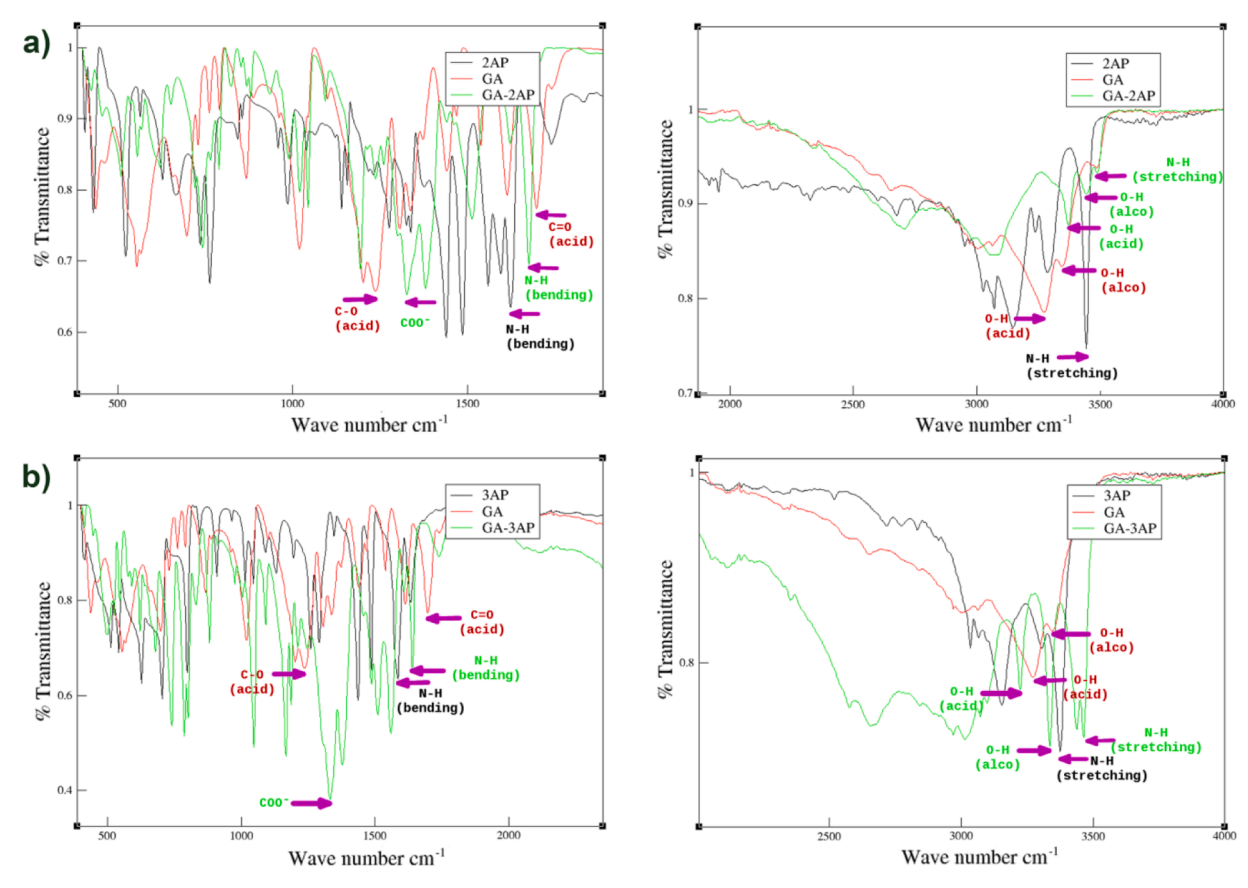


Fig. 3. FTIR spectra of a) GA-2AP and b) GA-3AP binary compounds along with respective pure compounds in the wavenumber range of 450–4000 cm<sup>-1</sup>.

 $\label{eq:table 1} \textbf{Table 1} \\ \textbf{FTIR major band assignment of starting and multicomponent compounds (cm$^{-1}$)}.$ 

Sample	ν <sub>O-H</sub> (Alcohol)	ν <sub>O-H</sub> (Acid)	$ u_{C=O} $ (Acid)	$ u_{C-O} $ (Acid)	$ u_{N-H} $ (Bending)	$ u_{N-H} $ (Stretching)
GA	3345.27	3273.45	1700.25	1239.40	-	-
2AP	-	-	-	-	1624.36	3447.63
3AP	-	-	-	-	1589.55	3379.40
GA-2AP	3449.98	3375.41	1326.67		1674.80	3493.34
GA-3AP	3340.72	3230.21	1332.22		1640.66	3470.57

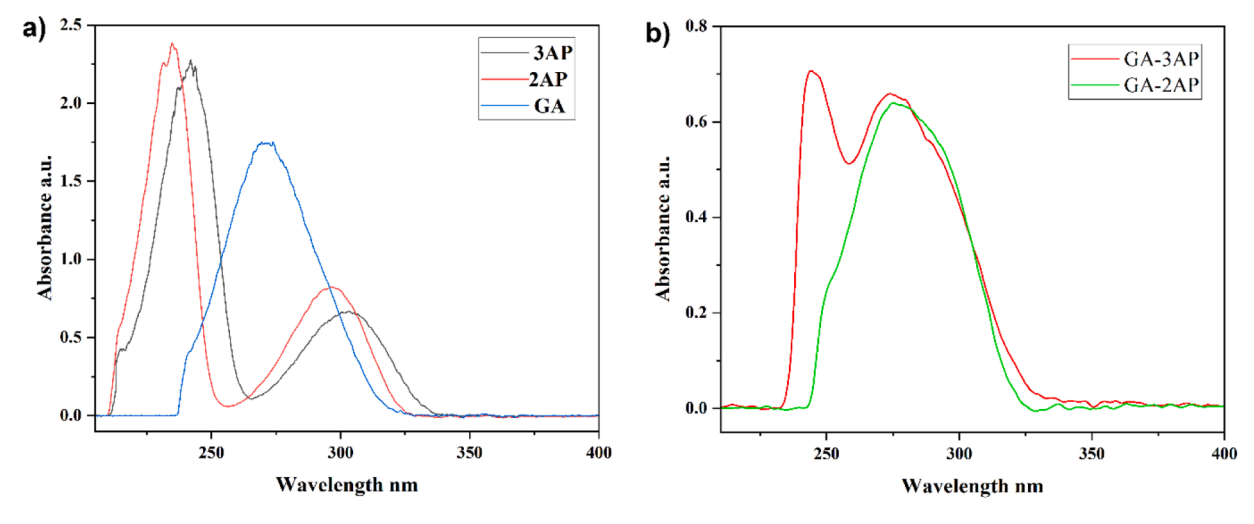


Fig. 4. Solid-State UV-Vis Spectra of a) initial compounds and b) binary compounds, to determine the band gap energy value.

**Table 2**Crystal data and structure refinement detail.

Parameter	GA-2AP molecular salt crystal	GA-3AP molecular salt crystal
Empirical formula	2(C <sub>7</sub> H <sub>5</sub> O <sub>5</sub> ) <sup>-</sup> .2(C <sub>5</sub> H <sub>7</sub> N <sub>2</sub> ) <sup>+</sup>	$(C_7H_5O_5)^(C_5H_7N_2)^+$
*	$[C_{24}H_{27}O_{10}N_4]$	$[C_{12}H_{13}O_5N_2]$
Formula weight	528.47	264.24
Temperature (K)	296(2)	296
Wavelength (Å) (CuKα)	1.54178	1.54178
Crystal system, space group	Monoclinic, P2 <sub>1</sub> /c	Monoclinic, P2 <sub>1</sub> /n
Unit cell dimensions $(\mathring{A}, \circ)$	a = 11.4550(3)	a = 9.4935(8)
	b = 13.3932(4)	b = 10.3154(2)
	c = 15.4683(5)	c = 11.9404(3)
	$\beta = 100.801(8)$	$\beta = 106.594(4)$
Volume (Å <sup>3</sup> ), Z	2331.09(3), 4	1120.62(10)
Density (g cm <sup>-3</sup> )	1.506	1.566
Absorption coefficient (mm <sup>-1</sup> )	1.013	1.054
$F_{000}$	1104	552.0
Crystal size (mm <sup>3</sup> )	$0.25\times0.12\times0.10$	$0.21\times0.20\times0.15$
$2\theta$ range for data collection	5.13° to 60.92°	5.77° to 65.12°
Index ranges	$-12 \leq h \leq 12$	$-11 \le h \le 11$
· ·	$-15 \le k \le 15$	$-12 \le k \le 12$
	$-17 \leq l \leq 17$	$-14 \leq l \leq 14$
Reflections collected	27362	13787
Independent reflections	3354 [ $R_{\text{int}} = 0.0257$ ]	1813 [ $R_{\text{int}} = 0.0357$ ]
Absorption correction	Multi-scan	Multi-scan
Refinement method	Full matrix least-squares on $F^2$	Full matrix least-squares on F <sup>2</sup>
Data/restraints/	3354/94/351	1813/0/178
parameters	1.104	1.004
Goodness-of-fit on F <sup>2</sup>	1.104	1.094
Final $[I > 2\sigma(I)]$	R1 = 0.1218,	R1 = 0.0399,
D: 1: (11.1.)	wR2 = 0.3935	wR2 = 0.1058
R indices (all data)	R1 = 0.1234	R1 = 0.0401
T + 4:00 1 4	wR2 = 0.3981	wR2 = 0.1060
Largest diff. peak and hole (e $Å^{-3}$ )	1.696 and -0.888	0.177 and -0.198
CCDC deposit No.	1906120	1902890

calculations were carried out by employing symmetry operations to generate molecular wave functions and to compute the electron densities of the cluster of title molecules present around the selected molecule using the CE-B3LYP/6-31G(d,p) energy model with the scale factors to determine  $E_{tot}$ :  $k_{ele}=1.057,\,k_{pol}=0.740,\,k_{dis}=0.871,\,k_{rep}=0.618.$ 

# 2.10. Enrichment ratio calculations

The enrichment ratios (E) of the molecular interactions assess the degree to which chemical entities present in a molecule form interaction in a crystalline environment. It is calculated as the ratio of actual contacts present in the crystal ( $C_{XY}$ ) to the random contacts as if all were equivalent ( $R_{XY}$ ), given by  $E_{XY} = \frac{C_{XY}}{R_{XY}}$  [64]. The pairs wherein the crystal environment support their high tendency to form intermolecular interactions has an E value of unity while for the pairs that does not support forming interactions, the E value is less than one.

#### 2.11. Density functional theory calculations

The density functional theory (DFT) is presently the most successful and promising approach to compute the electronic structure of the matter. This method was developed by Walter Kohn [65,66] and it predicts a great variety of molecular properties: molecular structures, vibrational frequencies, atomization energies, ionization energies, electric and magnetic properties, reaction paths. In its original formulation, the density functional theory provides the ground state properties of the system. In DFT method electronic charge density function  $\rho(\mathbf{r},\mathbf{t})$  (a

**Table 3** Hydrogen bond geometry of the reported molecular salt crystals.

Crystal (1) GA-2AP n	nolecular	salt cryst	tal		
D-H···A	D-H	H···A	D···A	D- H···A	Symmetry Code
O1-H1···O2 (intra)	0.82	2.52	2.914(3)	111	-
O1-H1···O10	0.82	1.89	2.701(3)	173	$2-x$ , $\frac{1}{2}+y$ , $3/2-z$
N1-H1BO4	0.86	1.98	2.829(40	170	-
O2-H2···O1 (intra)	0.82	2.52	2.914(3)	111	-
O2-H2···O10	0.82	1.91	2.729(3)	174	$2-x$ , $\frac{1}{2}+y$ , $3/2-z$
N2-H2A···O5	0.86	1.92	2.704(3)	152	-
N2-H2BO9	0.86	2.16	2.964(3)	156	x, $1/2 - y$ , $1/2 - z$
O3-H3···O2 (intra)	0.82	2.29	2.730(3)	114	-
O3-H3···O9	0.82	2.01	2.782(3)	157	$x$ , $3/2 - y$ , $\frac{1}{2} + z$
N3-H3A···O10	0.86	1.9	2.753(3)	169	-
N4-H4A…O9	0.86	2.03	2.848(3)	159	-
N4-H4B…O4	0.86	2.08	2.802(4)	141	1 - x, 1 - y, 1- z
O6-H6…O7 (intra)	0.82	2.27	2.708(3)	114	-
O6-H6···O1	0.82	2.03	2.790(3)	153	2 - x, 1 - y, 2- z
O7-H7···O5	0.82	1.85	2.628(3)	157	-
O7-H7O8 (intra)	0.82	2.43	2.772(3)	106	-
O8-H8···O3	0.82	2.09	2.906(3)	176	1-x, $-1/2+y$ , $3/2-z$
C1-H1A···O5 (intra)	0.93	2.43	2.755(3)	100	
C17-H17···O9 (intra)	0.93	2.47	2.778(3)	100	
C21- H21···O5	0.93	2.51	3.255(4)	137	x, y, -1 + z
C22-H22···O1	0.93	2.54	3.221(4)	126	2 - x, $1 - y$ , $1 - z$
Crystal (2) GA-3AP	molecul	ar salt cr	ystal		
D-H···A	D-H	H···A	DA	D- H…A	Symmetry Code
N8-H8O16	0.86	2.26	3.0550 (9)	154	-1/2+x,3/2-y,-1/2+z
N8-H8···O15	0.86	2.18	3.0307	169	-3/2+ <i>x</i> ,3/2- <i>y</i> ,-1/ 2+ <i>z</i>
O13-H13···O14 (intra)	0.86	2.27	2.7309	112	-
O13-H13···O14	0.86	2.17	2.8671 (7)	138	2-x,1-y,1-z
O14-H14···O16	0.83	1.90	2.6935	160	3/2- <i>x</i> ,-1/2+ <i>y</i> ,3/2- <i>z</i>
O15-H15O17	0.93	1.72	2.6529 (5)	175	1/2+x,3/2-y,1/ 2+z
N18-H18···O16	0.86	2.27	3.0200 (8)	146	-
N18-H18···O17	0.86	2.27	2.8550 (8)	151	-
C8-H8···O13	.93	2.40	3.2600	153	-1/2+x,3/2-y,1/2+z
C12-H12···O16	0.93	2.54	3.3170 (2)	141	-1/2+ <i>x</i> ,3/2- <i>y</i> ,-1/ 2+ <i>z</i>

function of three space variables (x,y,z) and time) of the many-body system is taken as a fundamental variable rather than the electronic wavefunction (which is a function of 3N space variables and time) of many-body system. Therefore, DFT method significantly speeds up the calculation and gives a direct relation between the charge density and the energy of the many-electron system. Since, here the energy of the system is expressed in terms of charge density functional  $E = E [\rho(r, t)]$ , called as density functional theory.

To determine the ground state electronic structure of the GA-2AP and GA-3AP molecular salt crystals, we carried out density functional theory (DFT) analysis using the hybrid exchange-correlation function with the basis set level of B3LYP/6-31G(d,p) using the Gaussian 16 program [67]. The global chemical properties of the molecular salt crystals were calculated using frontier molecular orbitals (HOMO and LUMO) using Koopman's theorem which is a simplified quantum mechanical approach that provides an estimate of the ionization potential, electronegativity, hardness and electron affinity of the molecules [68]. The molecular electrostatic potential (MEP) map highlights the regions of potential intermolecular interactions between different molecular components were also generated and analysed. The results were

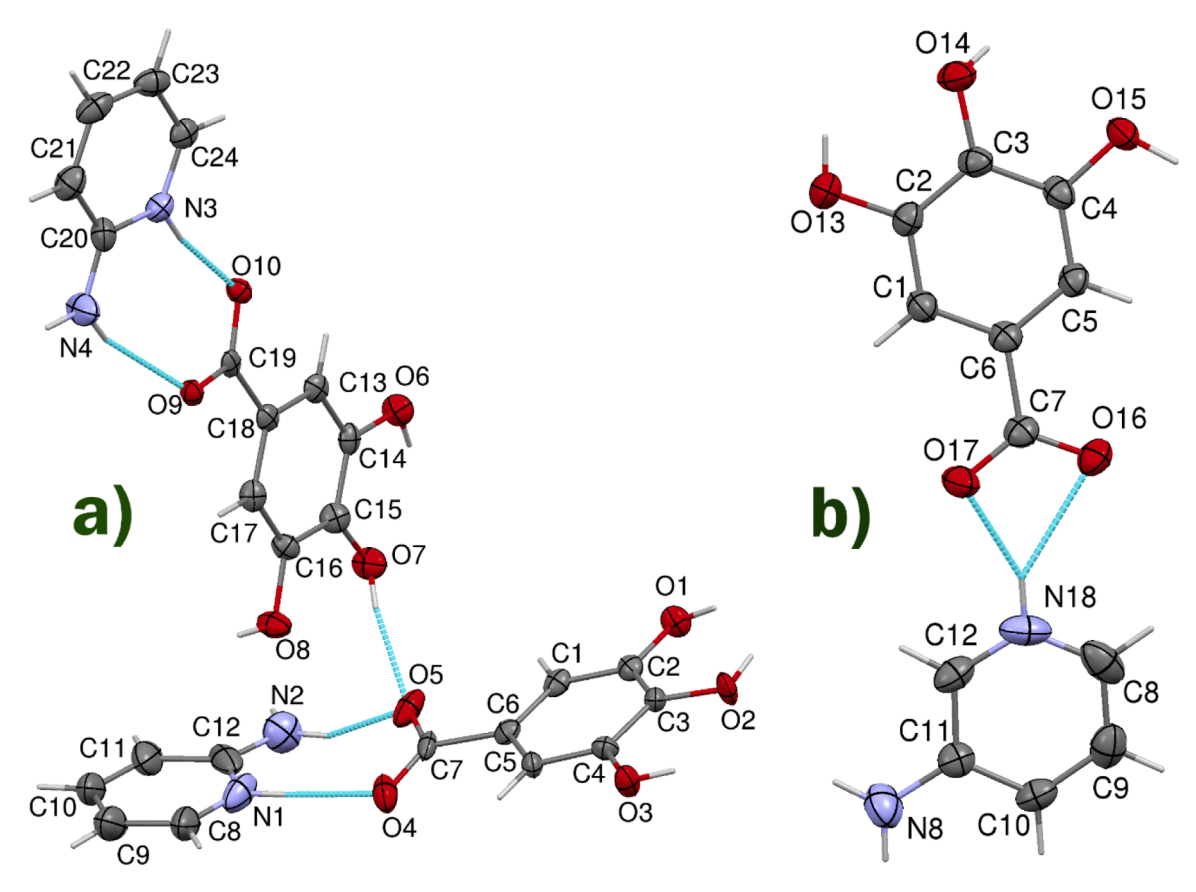


Fig. 5. ORTEP diagram of (a) 2:2 GA-2AP and (b) 1:1 GA-3AP molecular salt crystals drawn at 50% probability and non-hydrogen atoms are labelled. The molecules are connected through intermolecular hydrogen bonds (dotted lines).

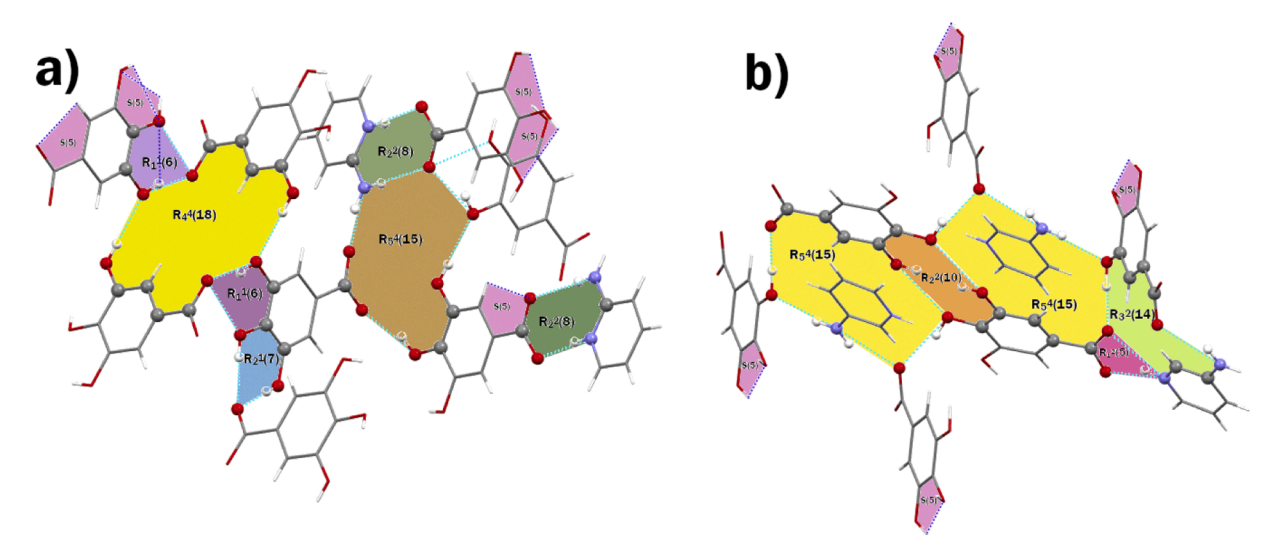


Fig. 6. supramolecular intra and inter molecular ring synthons in (a) GA-2AP and (b) GA-3AP molecular salt crystal structures.

visualised using gauss view 6.0.16 software [69].

# 2.12. Molecular docking studies

AutoDock Vina was used to carry out the molecular docking studies of the newly synthesised compounds [70]. The prime focus of our investigation was SARS-CoV-2. The target was selected by reviewing the previously published studies. The leading part of the target bio-macromolecular crystal structure of SARS-CoV-2: M pro (6LU7)

[70], pre-fusion spike glycoprotein with single receptor binding domain (6VSB) [71], SARS-CoV-2 spike ectodomain structure (open state) (6VYB) [72] were downloaded from the PDB database. Water molecules were eliminated and polar hydrogens were added to prepare the protein. The Lamarckian Genetic Algorithm (LGA) was used as the AutoDock suite [73]. The docking data and binding site were analysed using the output file. The docking results and interaction poses were generated using Discovery Studio [74].

**Table 4** Geometrical parameters of  $\pi...\pi$  interactions in GA-2AP and GA-3AP molecular salt crystals.

Cg(I) - Cg(J)	Cg⋯Cg in Å	α	β	γ	CgI-Perp	CgJ-Perp	Symmetry code
Crystal (1) GA-2AF	P molecular salt crystal						
Cg(1) - Cg(3)	4.217(2)	12.81(16)	28.8	41.6	-3.1550(10)	-3.6958(16)	1-x,1/2+y,3/2-z
Cg(1) - Cg(3)	3.7989(19)	14.17(16)	4.1	16.1	3.6501(10)	3.7892(16)	1-x,1-y,2-z
Cg(2) - Cg(4)	4.7507(16)	9.94(12)	42.6	52.0	2.9241(10)	3.4957(11)	2-x,1-y,1-z
Cg(2) - Cg(4)	3.7991(15)	7.67(12)	22.5	17.8	-3.6169(10)	-3.5090(11)	x,1/2-y,1/2+z
Crystal (2) GA-3AF	P molecular salt crystal						
Cg(1) - Cg(2)	3.6044(9)	13.87(7)	14.1	28.0	-3.1823(6)	3.4953(6)	1+x,y,z
Cg(2) - Cg(1)	3.6045(9)	13.87(7)	28.0	14.1	3.4953(6)	-3.1823(6)	-1+x,y,z
Cg(2) - Cg(2)	3.3930(9)	0	17.4	17.4	3.2372(6)	3.2372(6)	-x,2-y,1-z

#### 3. Results and discussion

#### 3.1. Powder X-ray diffraction

PXRD is a readily available technique generally used for the confirmation of interaction between the starting compounds and to check the crystallinity of the bulk material [20]. Also, PXRD provides fundamental structural information on the material. The PXRD diffractograms of the initial compounds and cogrinding products of both GA-2AP and GA-3AP are shown in the Fig. 2. Characteristic high intense peaks were selected and their  $2\theta$  values are recorded. For these selected peaks position, (hkl) values were calculated and labelled in Figs. S1 and S2. The pure compounds have characteristic diffraction peaks at  $2\theta$  positions  $8.096^{\circ}$ , 11.901°, 16.210° (highest intensity peak), 19.160°, 25.404°, 27.730°, 28.019° in case of GA, 7.789°, 15.357° (highest intensity peak), 30.562°, 30.822° in case of 2AP, and 14.185°, 20.247°, 22.444°, 23.253° (highest intensity peak), 28.689° in case of 3AP respectively. The appearance of numerous new diffraction peaks at  $2\theta$  positions  $14.895^{\circ}$ ,  $18.895^{\circ}$ , 23.870°, 26.758°, 27.348° in PXRD pattern of GA-2AP and at  $2\theta$  positions 17.649°, 19.700°, 25.499°, 26.992°, 27.981°, 30.375° in PXRD pattern of GA-3AP and also the disappearance of characteristic diffraction peaks of the starting compounds in these binary compounds has clearly illustrated the formation of new crystalline phases. Further, simulated PXRD patterns of GA-2AP and GA-3AP crystals obtained from the single-crystal X-ray diffraction data, were also shown in the Fig. 2.

# 3.2. Fourier transform infra-red spectroscopy

An FTIR spectroscopic study was performed to identify the noncovalent interactions within the molecular salt. A shift in the carbonyl group of the acid is common when the group is involved in intermolecular interactions [21]. The FTIR spectra of the starting compounds and the reported binary compounds were drawn using the experimental data and analysed (Fig. 3). The wavenumber of the characteristic transmittance peak representing the functional groups of the compounds were assigned, compared and listed in Table 1. The shift in the characteristic transmittance peaks and the presence of new peaks in the reported compounds are due to the formation of hydrogen bonds between the molecules of the starting compounds. Interesting results were also observed from the analysis of the experimental FTIR data. The presence of two major absorption bands namely, C=O stretching band at 1700.25 cm<sup>-1</sup> and C-O stretching band at 1239.40 cm<sup>-1</sup> in the FTIR spectra of GA demonstrates the presence of carboxylic acid group. These two bands were not found in the FTIR spectra of GA-2AP and GA-3AP compounds. Instead, single absorption band was found at  $1326.67~\mathrm{cm}^{-1}$  and 1332.22cm<sup>-1</sup> in GA-2AP and GA-3AP binary compounds respectively. This demonstrated the presence of carboxylate anion (-COO-) and also proved the transfer of proton from the carboxylic acid group of the binary compounds. This observation has confirmed that, the binary compounds were crystallized as molecular salts. Furthermore, the proton transfer and molecular salt formation was again confirmed by measuring the bond lengths bond length of C-O groups in the carboxylate anion (-COO<sup>-</sup>) using the SCXRD data of the reported compounds.

#### 3.3. Solid-State UV-Vis Spectrum

The solid-state UV-Vis absorption spectrum of initial compounds (GA, 2AP and 3AP) and the binary compounds (GA-2AP and GA-3AP) are shown in Fig. 4. The experimental solid-state UV-Vis absorption spectrum of the initial compounds were found to be different from that of the binary compounds. This indicates the formation of interaction between the compounds through intermolecular interaction and confirms the formation of binary compounds. The band gap energy values were calculated using the wavelength values at which maximum absorption is taking place. Experimental band gap energy values in eV for GA, 2AP and 3AP were found to be 4.628, 5.363, and 5.133 respectively, while that of the GA-2AP, GA-3AP binary compounds were found to be 4.5170 and 5.0805 respectively. These results shows that both the binary compounds are more reactive and less stable than the respective coformers (2AP and 3AP).

#### 3.4. Crystal structure description

Transparent block shaped GA-2AP and light brown colored cuboid shaped GA-3AP crystals, suitable to collect X-ray diffraction intensity data were selected using a polarised microscope, and the crystal structures were solved. The crystals were found to be crystallized in a monoclinic system with  $P2_1/c$  and  $P2_1/n$  space groups respectively. Overall 351 and 178 parameters were refined with 3354 and 1813 unique reflections converged to residual in solving the two crystal structures respectively. The GA-2AP compound was found to be crystallized in 2:2 and GA-3AP compound was found to be crystallized 1:1 stochiometry. The summary of crystal data and refinment parameters of the both binary crystals were given in the Table 2. The parameters of various inter and intramolecular hydrogen bond interactions responsible for the formation of these two molecular salt crystals are listed in the Table 3. Full crystallographic tables (including structure factors) of the crystals have been deposited with the Cambridge Crystallographic Data Centre (CCDC) as supplementary publication numbers 1906120 and 1902890.

#### Crystal structure of GA-2AP:

The asymmetric unit of 2:2 GA-2AP crystal is found to have two ring dimers between GA and 2AP molecules which are connected through a double hetero nuclear hydrogen bonds of the type N-H···O resultin in the formation of two  $R_2^2(8)$  homosynthons. Further these two ring synthons were connected through C-H···O tpye hydrogen bond interaction as shown in the Fig. 5. From the structure analysis we also noticed the transfer of proton from the carboxyl group of the GA molecules from O4 and O9 atoms to N1 and N4 atoms of the amine groups of 2AP molecules respectively. This proton transfer converted the neutral carboxylic acid of the GA molecules into carboxylate anions and neutral 2AP molecules into cations, resulting in the formation of ionic [COO-...H-N+] interactions. The proton transfer is also verified by the very small  $\Delta D_{\text{C-O}}$ values (0.015 Å and 0.016 Å) between C7-O4 and C7-O5 bond lengths and C19-O9 and C19-O10 respectively. Thus the presence of ionic molecules in the crystal structure of 2:2 GA-2AP has confirmed its formation as a molecular salt molecule.

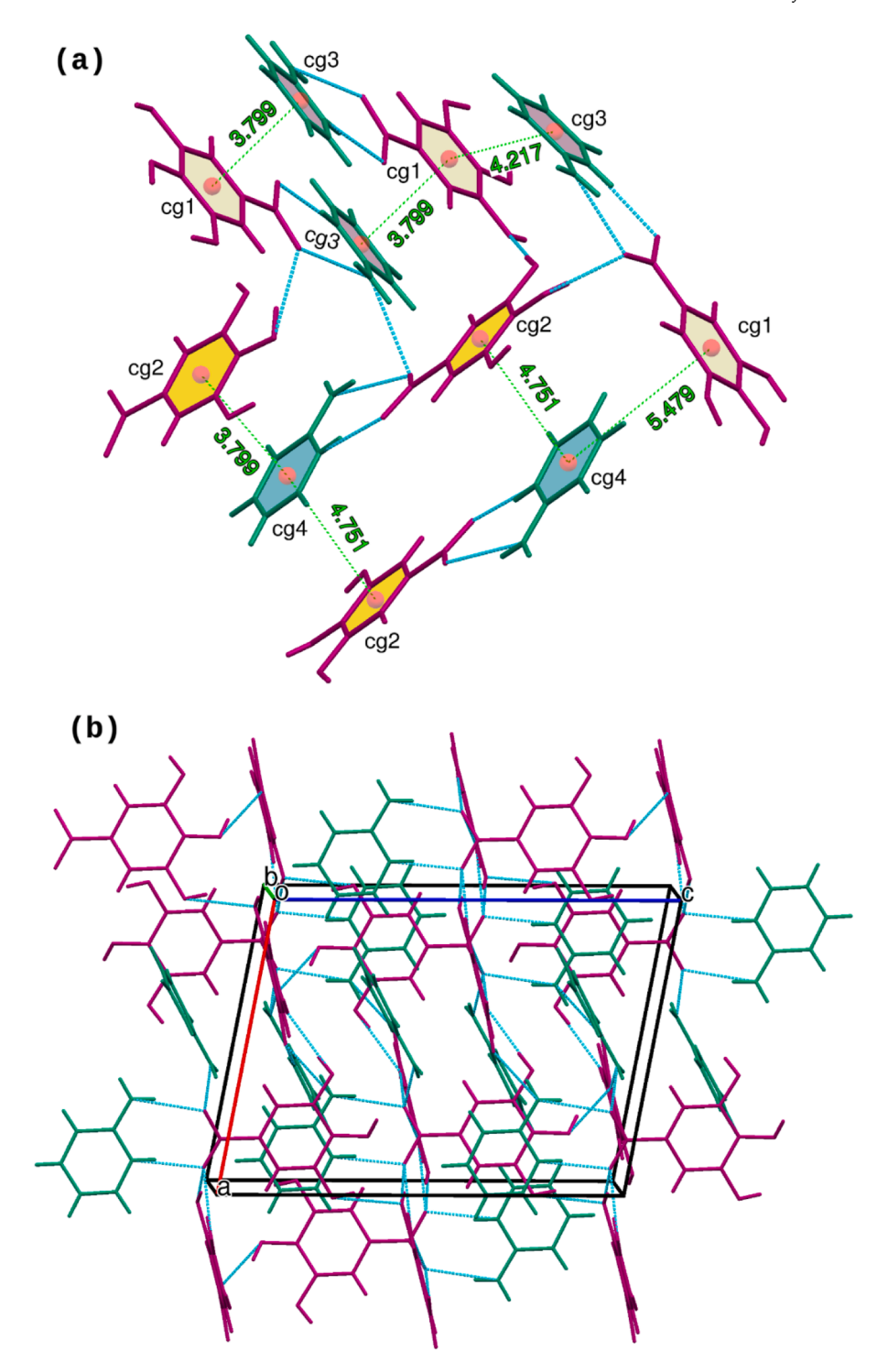


Fig. 7. (a) π···π stacking interactions in the 2:2 GA-2AP molecule and (b) packing of the molecules when viewed down the crystallographic b-axis.

From the analysis of inter and intramolecular hydrogen bond interactions which contributed to the formation of GA-2AP molecular salt, the formation of five S(5) ring synthons by the involvement of the hydroxyl groups through intramolecular hydrogen bonding interactions of the type O–H···O and two S(5) synthons through intramolecular hydrogen bonding interactions of the type C–H···O were identified in the crystal structure. Further, strong intermolecular interactions of the type O-H···O, N-H···O, and comparitively weak intermolecular interactions of the type C-H···O were contributed in the formation GA-2AP molcule and the details are shown in the Table 3. These intermolecular interactions were found involved in the formation of ring synthons with

graph set notation  $R_1^1(6)$ ,  $R_2^1(7)$ ,  $R_4^4(18)$ ,  $R_5^4(15)$ , and contributed towards the stability of the crystal structure (Fig. 6(a)). Detailed structural study of GA-2AP crystal has shown the presence of eight distinct and prominant  $\pi\cdots\pi$  interactions (Table 4) between the centroids of the six membered rings; Cg(1) of GA1 molecule (made up of atoms C1 to C6), Cg(2) of GA2 molecule (made up of atoms C13 to C18), Cg(3) of 2AP1 molecule (made up of atoms N1, C8 to C12), and Cg(4) of 2AP2 molecule (made up of atoms N3, C20 to C24). Fig. 7(a) shows how these interactions play major role in connecting the molecules thereby contributing towards the stability of the crystal structure. Further, Fig. 7 (b) shows the packing of the molecules in the unit cell when viewed

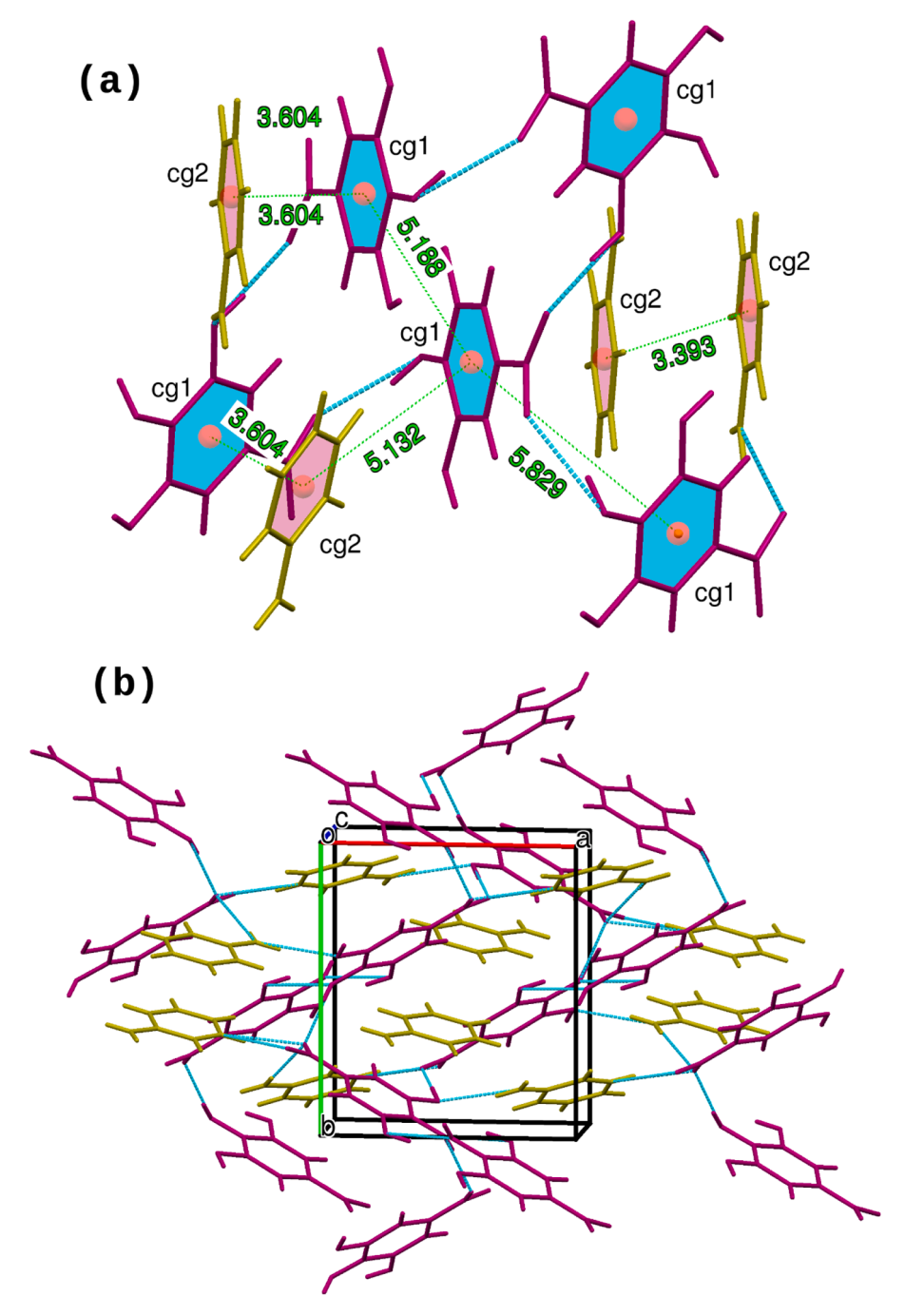


Fig. 8. (a) π···π stacking interactions in the 1:1 GA-3AP molecule and (b) packing of the molecules when viewed down the crystallographic c-axis.

down the crystallographic *b*-axis.

# Crystal structure of GA-3AP:

In the asymmetric unit of GA-3AP crystal, GA molecule is found to be connected to 3AP molecule through N18-H18…O16 and N18-H18…O17 hydrogen bond interactions resulting in the formation of  $\it R_1^2(5)$  ring motif. Further a very small difference of  $\Delta D_{C\cdot O}{=}0.004$  Å between the two bonds lengths; C7-O16(1.257 Å) and C7-O17(1.261 Å) has confirmed the proton transfer from O16 atom to N18 atom and hence the formation of molecular salt.

Further, the presence of strong intermolecular interactions of the type O-H···O and N-H···O, comparatively weak intermolecular interactions of the type C-H···O were found to be contributed in the formation of GA-3AP crystal. The detailed study of the crystal structure has revealed that, these interactions were involved in the formation of ring

synthons with graph set notation  $R_1^2(15)$ ,  $R_2^2(10)$ ,  $R_5^2(15)$ ,  $R_3^2(14)$ , and contributed towards the stability of the crystal structure (Fig. 6(b)). Furthermore, the presence of six distinct and prominant  $\pi \cdots \pi$  interactions (Table 4) between the centroids of the six membered rings (Fig. 8(a)); Cg(1) of GA molecule (made up of atoms C1 to C6), Cg(2) of 3AP molecule (made up of atoms N18, C8 to C12) and one lone pair··· $\pi$  interaction; C9-H9···Cg(1) with C9–Cg(1) distance of 3.8244 Å (symmetry; 1/2-x,1/2+y,3/2-z). Fig. 8(b) shows the packing of the molecules in the unit cell when viewed down the crystallographic c-axis.

#### 3.5. Thermogravimetric analysis

Thermograms of GA-2AP and GA-3AP crystals reflects their thermal properties and are as shown in the Fig. 9. One step thermogram of the

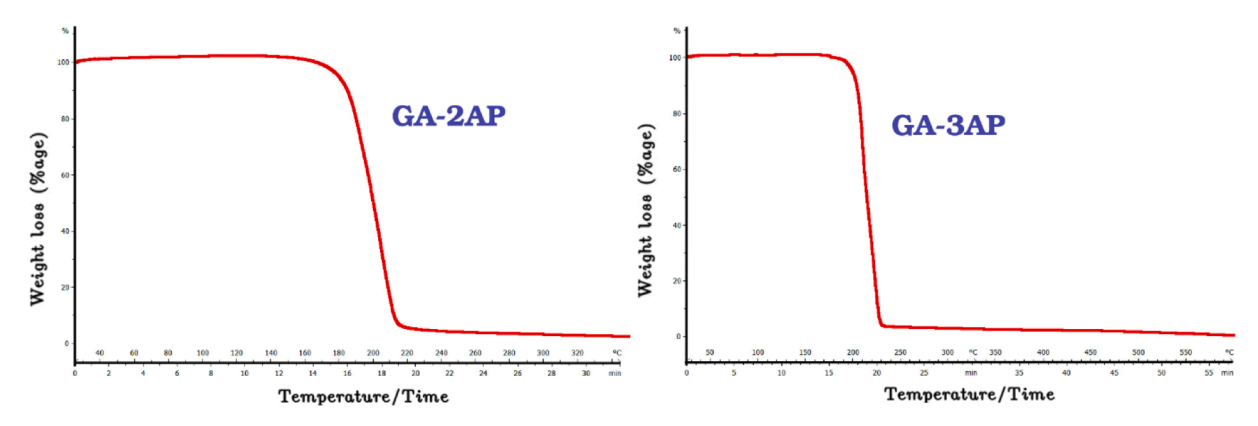


Fig. 9. TRA curve of a) GA-2AP and b) GA-3AP molecular salt crystals.

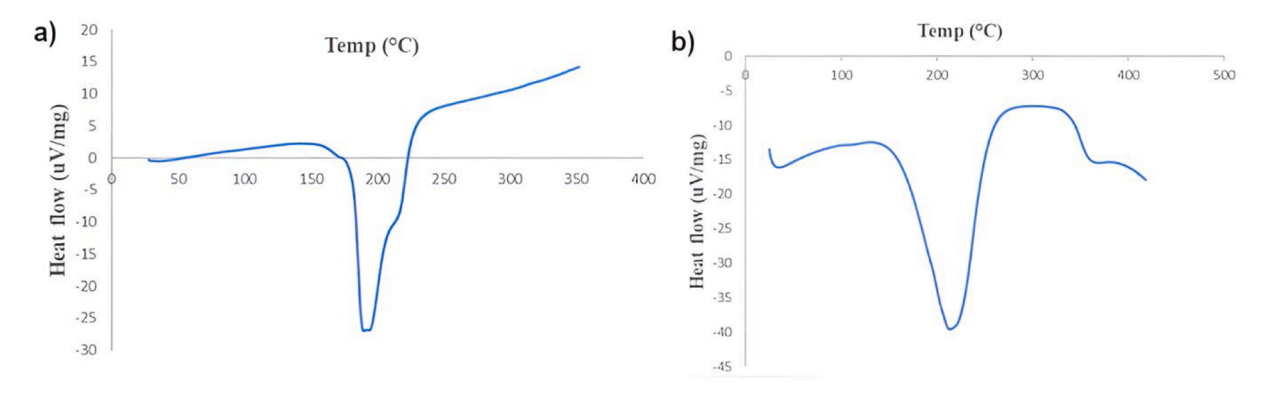


Fig. 10. Differential Thermal Analysis (DTA) curves for a) GA-2AP and b) GA-3AP molecular salt crystals, showing sharp endothermic peaks corresponding to their melting points.

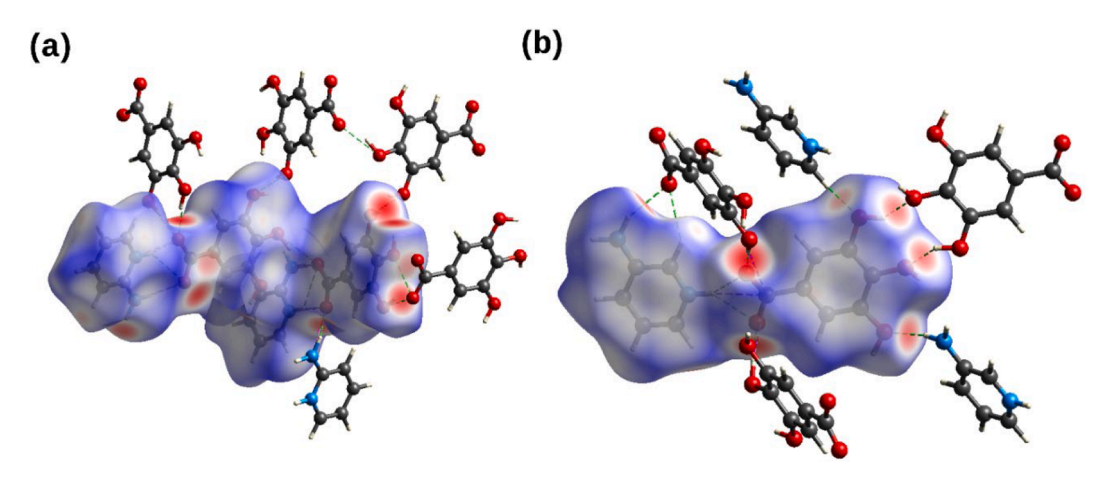


Fig. 11. The  $d_{\text{norm}}$  mapped Hirshfeld surface of (a) 2:2 GA-2AP molecular salt, and (b) 1:1 GA-3AP molecular salt.

crystals shows that they are thermally stable up to 155°C and 175°C respectively. A major weight loss (96%) observed between 155°C and 210°C temperatures in GA-2AP suggests that the crystal first melts and then decomposes gradually. Whereas a major weight loss (98%) between temperatures 175°C and 230°C in case of the GA-3AP crystal also indicates that the crystal first melts and then decomposes gradually [75]. Attractively here the melting temperature has been decreased by taking GA (250°C) in binary component form with 2AP and 3AP. This decrease in the melting temperature may support the improvement the solubility.

#### 3.6. Differential Thermal Analysis (DTA)

The DTA curves for the GA-2AP and GA-3AP molecular salt crystals are depicted in Fig. 10. The thermogram for GA-2AP (Fig. 10a) exhibits a single, sharp endothermic peak centered at 193°C. This distinct thermal event is attributed to the melting of the crystalline salt. Similarly, the DTA curve for GA-3AP (Fig. 10b) shows a sharp endotherm at a higher temperature of 213°C corresponding to its melting point. The sharpness of these peaks indicates a high degree of crystallinity for both materials. Furthermore, these melting points are consistent with the initial decomposition temperatures observed in the thermogravimetric analysis (TGA), confirming the phase transition temperatures of the

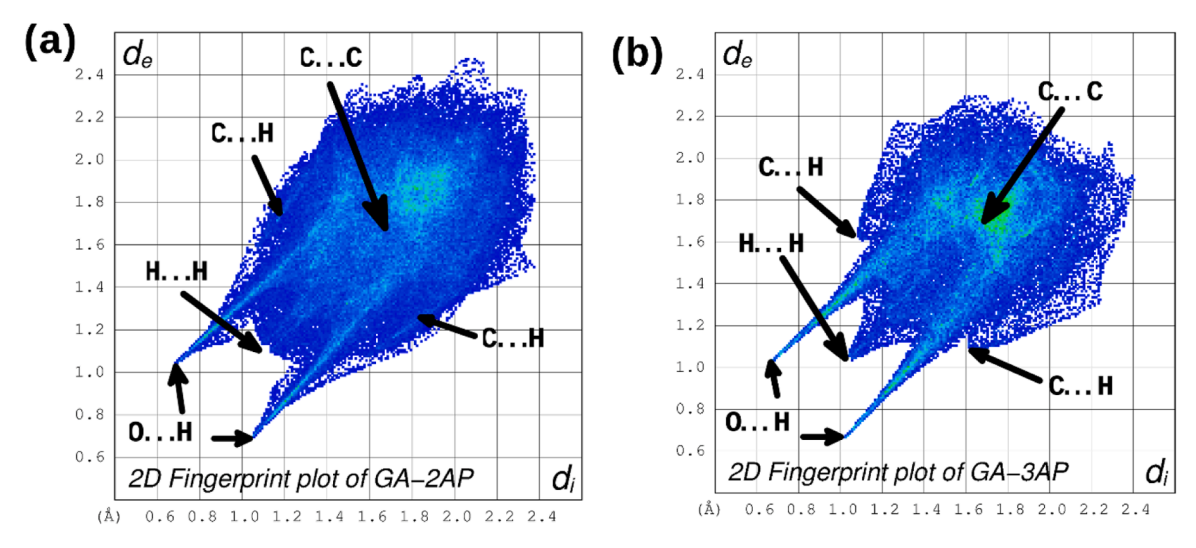


Fig. 12. Overall 2D fingerprint plot of (a) 2:2 GA-2AP molecular salt, and (b) 1:1 GA-3AP molecular salt.

Table 5 Molecular interaction energies of molecular salt crystals around the radius of 3.8 Å in kJ mol<sup>-1</sup>. [Scale factors,  $k_{ele} = 1.057$ ;  $k_{pol} = 0.74$ ;  $k_{dis} = 0.871$  and  $k_{rep} = 0.618$  were used].

Crystal	$E_{ele}$	$E_{pol}$	$E_{dis}$	$E_{rep}$	$E_{tot}$	$E_{tot-sum}$
GA-2AP	-544.672	-492.618	-208.082	780.9666	-467.1	-464.4054
GA-3AP	-584.944	-310.356	-121.679	247.4472	-770.2	-769.5318

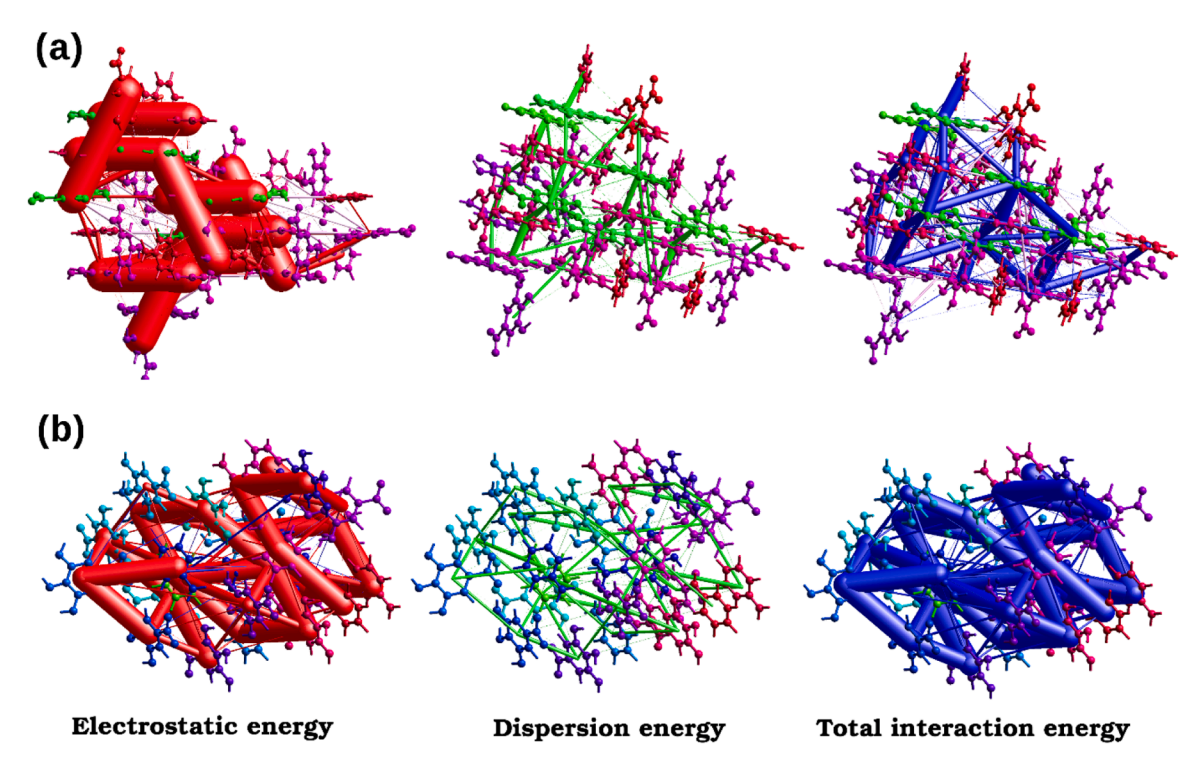


Fig. 13. 3D electrostatic, dispersion, and total interaction energy frameworks of (a) 2:2 GA-2AP molecular salt, and (b) 1:1 GA-3AP molecular salt with tube size 100. Tube thickness indicates the interaction energy value (the thicker the tube the greater the energy).

molecular salts [76].

# 3.7. Hirshfeld surface analysis

Analysing the Hirshfeld surface of the reported binary crystals enables us to identify and quantify the critical intermolecular interactions,

such as hydrogen bonds, van der Waals forces, and electrostatic interactions, which significantly influence the material's structural and electronic features. The three-dimensional  $d_{\rm norm}$  surface of GA-2AP was drawn with color scale in between -0.6877 au (red) to 1.2655 au (blue) and that of GA-3AP was drawn with color scale in between -0.7292 au (red) to 1.0539 au (blue) as shown in the Fig. 11. The calculated volume

**Table 6**Hirshfeld surface contacts, the derived random contacts and ER values for GA-2AP.

Contacts (%)						
Atoms	O	Н	N	С		
0	0.8	-	-	-		
H	29.5	37.9	-	-		
N	0.2	1.9	0	-		
C	3.6	16.6	2.0	7.4		
Surface %	17.45	61.9	2.05	18.5		
Random Contac	ets (%)					
0	3.04	-	-	-		
H	21.60	38.22	-	-		
N	0.71	2.53	0.04	-		
C	6.45	22.9	0.76	3.42		
<b>Enrichment Rat</b>	rio E <sub>XY</sub>					
0	0.26	-	-	-		
H	1.37	0.99	-	-		
N	-	0.75	-	-		
C	0.56	0.72	-	2.16		

**Table 7**Hirshfeld surface contacts, the derived random contacts and ER values for GA-3AP.

Contacts (%)							
Atoms	0	Н	N	С			
0	1.2	-	-	-			
H	33.1	34.9	-	-			
N	0.7	1.5	0.1	-			
C	2.8	15.9	2.2	7.4			
Surface %	19.5	60.15	2.3	17.85			
Random Contac	cts (%)						
0	3.80	-	-	-			
H	23.46	36.18	-	-			
N	0.89	2.77	0.05	-			
C	6.96	21.47	0.82	3.19			
Enrichment Rat	Enrichment Ratio Exy						
0	0.32	-	-	-			
H	1.41	0.96	-	-			
N	0.79	0.54	-	-			
С	0.40	0.74	-	2.32			

of the Hirshfeld surface of GA-2AP is 572.05 ų in the area of 535.59 Ų with a globularity index of 0.622 and an asphericity index of 0.204. Whereas, the calculated volume of the Hirshfeld surface of GA-3AP is 273.71 ų in the area of 283.82 Ų with a globularity index of 0.718 and an asphericity index of 0.40. The deep red colored regions highlights the short-range interactions such as hydrogen bonding, while the blue regions correspond to longer-range contacts like O···H, H···H and other possible interactions.

The analysis of 2D fingerprint plot gives the quantitative contributions of molecular contacts to the total Hirshfeld surface. The 2D fingerprint plots of the binary crystals were displayed in the range of 0.6 - 2.4 Å view with the  $d_{\rm e}$  and  $d_{\rm i}$  distance scales displayed on the graph axes (Fig. 12). Where  $d_{\rm e}$  and  $d_{\rm i}$  are the distances to the nearest nuclei outside and inside the surface from the Hirshfeld surface respectively.

In both GA-2AP and GA-3AP crystals, the H···H contacts have maximum (37.9% & 34.9%) and N···N has minimum (0.0% & 0.1%) contributions. The second highest contribution is from O···H (29.5% & 33.1) respectively and are represented by a pair of sharp spikes with almost same value of  $d_{\rm e}+d_{\rm i}$ . The next highest contribution is from C···H (16.6% & 15.9%) contacts respectively, and were seen in the form of butterfly pattern on the 2D fingerprint plots. The significant C···C contacts have contributed 7.4% in both the crystals and were appeared in form of fish shaped pattern on the fingerprint plots. The remaining, O···C (3.6% & 2.8%), N···C (2.0% & 2.2%), N···H (1.9% & 1.5%), O···O

Table 8
HOMO/LUMO energy and related molecular properties of TY, GA and TY-GA cocrystal hydrate.

Parameter	GA	2AP	3AP	GA- 2AP	GA- 3AP
$E_{HOMO}$ (eV) $E_{LUMO}$ (eV) Energy gap ( $\Delta$ ) (eV) Ionization energy (I) (eV) Electron affinity ( $\Lambda$ ) (eV) Electronegativity ( $\chi$ ) (eV) Chemical potential ( $\mu$ ) (eV)	-6.7101 -1.8471 <b>4.8629</b> 6.7101 1.8471 4.2786 -4.2786	-6.1269 -0.8446 <b>5.2823</b> 6.1269 0.8446 3.4858 -3.4858	-6.1484 -0.9358 <b>5.2126</b> 6.1484 0.9358 3.5421 -3.5421	-6.0173 -1.7415 <b>4.2757</b> 6.0173 1.7415 3.8794 -3.8794	-6.4733 -1.3002 <b>5.1732</b> 6.4733 1.3002 3.8867 -3.8867
Global hardness $(\eta)$ (eV) Global softness (s) $(eV^{-1})$ Electrophilicity index $(\omega)$ (eV)	2.4315 0.4113 3.7644	2.6411 0.3786 2.3003	2.6063 0.3837 2.4070	2.1379 0.4678 3.5198	2.5866 0.3866 2.9202

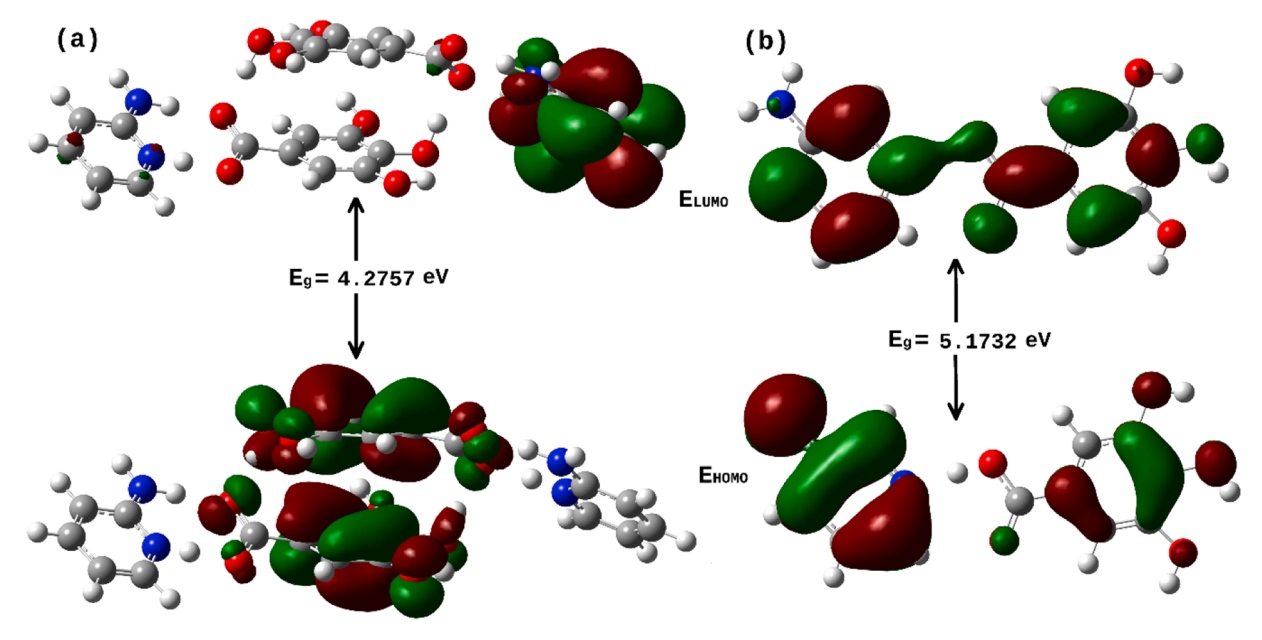


Fig. 14. Frontier molecular orbitals of (a) GA-2AP and (b) GA-3AP along with their energy gap.

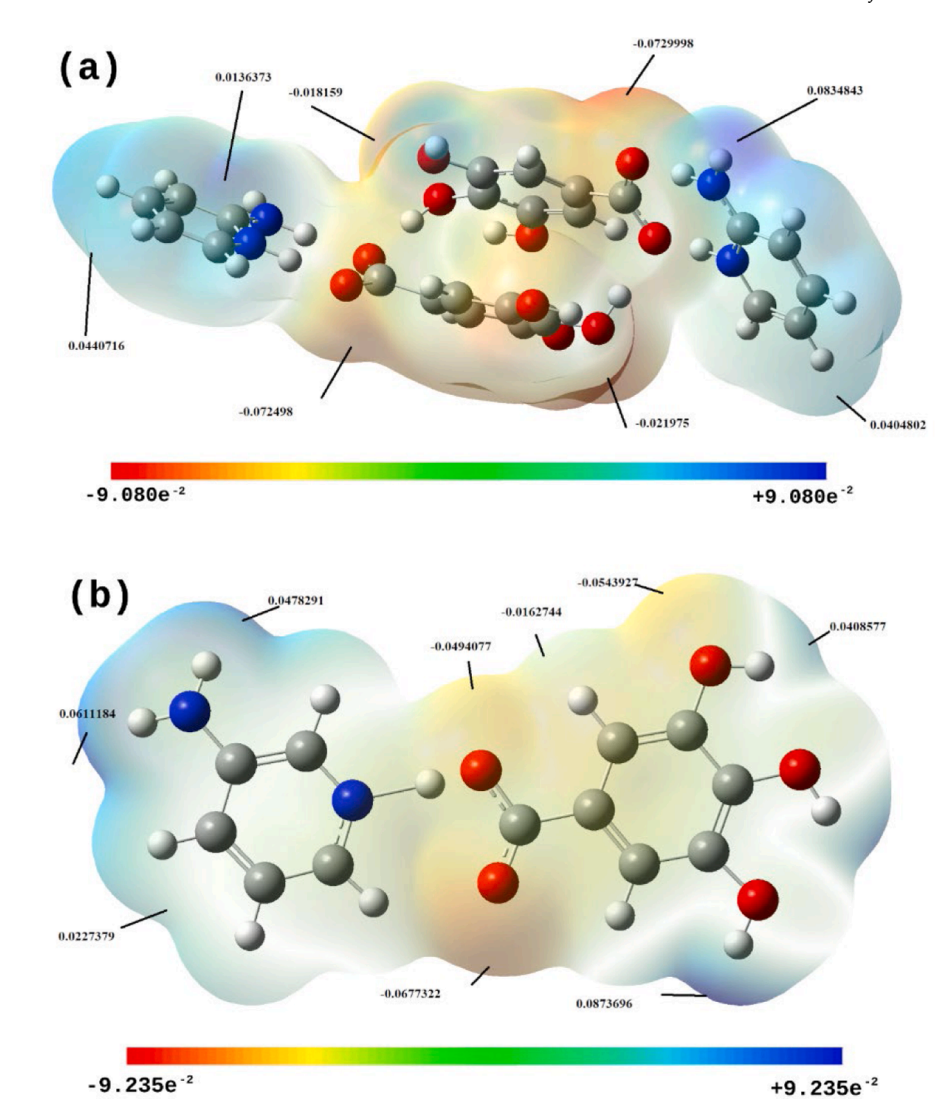


Fig. 15. Molecular electrostatic potential map of (a) GA-2AP and (b) GA-3AP molecular salt binary compounds.

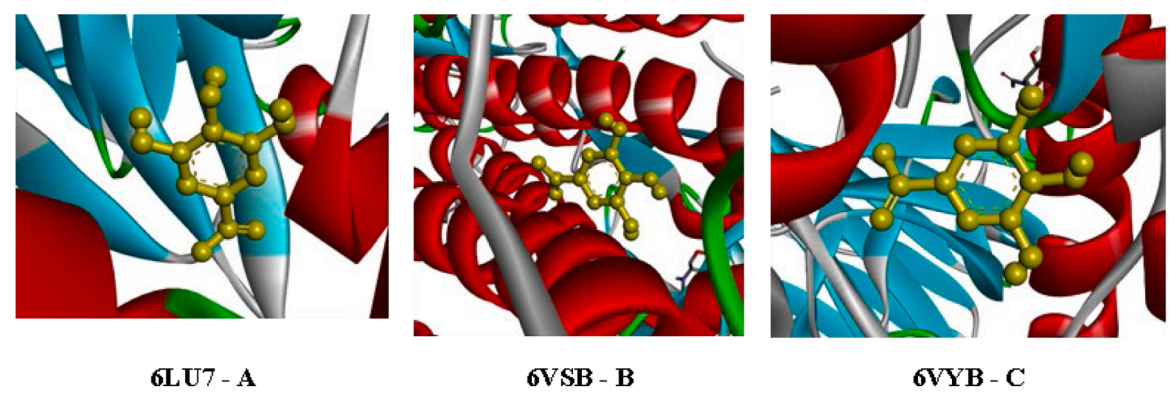


Fig. 16. 3D visualisation of the receptor-ligand interactions of GA-2AP.

(0.8% & 1.2%), and O···N (0.2% & 0.7%) contacts also contributed to the total area of the Hirshfeld surfaces of GA-2AP and GA-3AP crystals respectively (Figs. S3 and S4).

# 3.8. Interaction energies and energy frameworks

As energy frameworks indicate the directionality and strength of

main interactions present in a crystal lattice [77], various interactions energies between molecular pairs namely; electrostatic, dispersive, polarization and repulsion were computed using CRYSTALEXPLORER. The relative contributions these energies were realised and compared. Further, interaction energy framework calculations were carried out by employing symmetry operations to generate molecular wave functions. The crystallographic symmetry operations and their corresponding

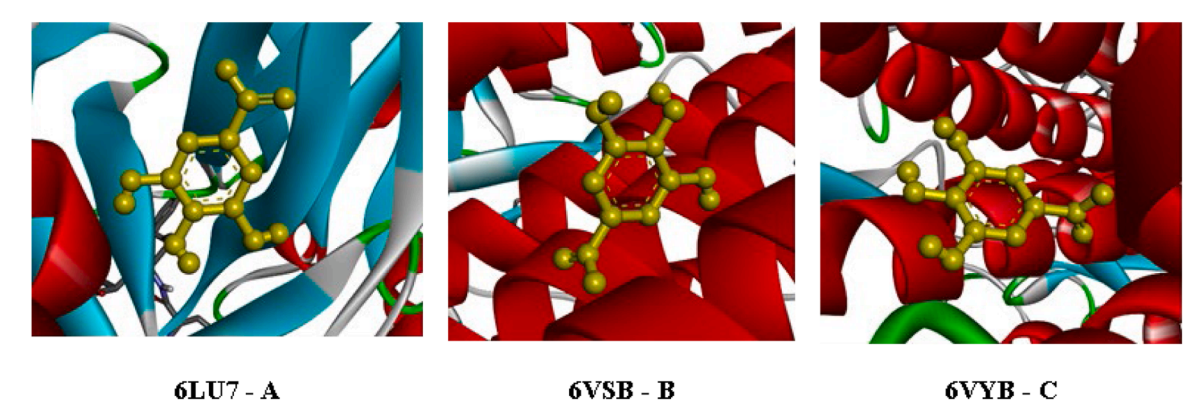


Fig. 17. 3D visualisation of the receptor-ligand interactions of GA-3AP.

molecular interaction energies (where R is the distance between molecular centroids (mean atomic position) in Å and N is the number of molecules at that distance, energies are in kJ  $\mathrm{mol}^{-1}$ ) are tabulated in **Table S1** and **Table S2** for GA-2AP and GA-3AP molecular salts respectively.

The case of GA-2AP molecule, light blue colored molecule located at a distance of 6.35 Å from the centroid of the selected molecule has shown the highest total interaction energy of -84.4 kJ mol<sup>-1</sup>. Whereas in the case GA-3AP, the red colored molecule with symmetry operation (x+1/2, -y+1/2, z+1/2) located at a distance of 6.85 Å from the centroid of the selected molecule has shown the highest total interaction energy of -91.9 kJ mol<sup>-1</sup>. Molecular interaction energy values were tabulated in Table 5. It was observed that, the sum of the four energy components  $(E_{tot-sum})$  are identical with the calculated total interaction energy  $(E_{tot})$ . In both the reported molecular salt crystals, the electrostatic energy is dominating over the dispersion and polarization energies. This is due to the ionic nature of the compounds.

The energy frameworks of the compounds were generated for electrostatic, dispersion and the total energy terms and represented in terms of different colored cylinders with scale factor (cylinder tube size) of 100 and cutoff energy -50 kJ/mol. These cylinders represent the magnitude of the interaction energy between molecular pairs and the strength of the molecular packing along different directions. The molecular cluster with the red cylinders represents the electrostatic energy ( $E_{\rm elec}$ ), the green color cylinders represent dispersive energy ( $E_{\rm dis}$ ) and the blue cylinders represent the total interaction energy (Fig. 13). The energy framework calculations revealed that the electrostatic energy dominates over the dispersion and polarization energies of the molecules in the crystalline environment of both the crystalls.

# 3.9. Enrichment ratio calculations

To explore the most likely interaction in the crystal structures, the enrichment ratio analysis was performed. The enrichment ratios calculated from the surface contacts for both the compounds is listed in Tables 6 and 7. The random contacts value less than 0.8% is neglected. In both the compounds C...C contacts are more favoured due to the extensive  $\pi$ - $\pi$  stacking interactions present. O...H contacts are also favoured in both the crystals with E values 1.37 and 1.41 for GA-2AP and GA-3AP respectively. This indicates that O-H hydrogen bond interactions dominate in both crystals and stabilises them. Even though H...H contacts contribute the most to the surface, these contacts are favoured in both the crystals marginally as the E value is near to 0.9. This is due to the pre-existing enrichment of H atoms in the O...H contacts. Self-contacts are impoverished in the case of N and O [77].

# 3.10. Density functional theory calculations

The geometry optimization of GA-2AP and GA-3AP compounds were

carried out using Gaussian 16 series of program by using the coordinates extracted from the corresponding cif files at B3LYP/6-31G (d,p) level of theory. Optimized structures of the title compounds are shown in Figs. S5 & S6. The theoretically predicted geometrical parameters (bond lengths, bond angles and torsion angles) with experimental values are given in Tables S3-S8. The comparison shows that optimized structures are very much similar to X-ray structures with correlation coefficient 0.9552, 0.9549 and 0.9949 for 2:2 GA-2AP whereas in case of 1:1 GA-3AP the correlation coefficient are 0.9257, 0.8745 and 0.9860 respectively. The theoretical bond lengths O4-C7, O5-C7, N1-C12 and N2-C12 of GA-2AP molecule are deviated by 0.005Å, 0.005Å, 0.022Å and 0.036Å respectively from the XRD results is due to proton transfer from GA1 molecule to 2AP1 molecule. Further, the theoretical bond lengths O9-C19, O10-C19, N3-C20 and N4-C20 of GA-2AP molecule are deviated by 0.015Å, 0.005Å, 0.013Å and 0.015Å respectively from the XRD results is also due to proton transfer from GA2 molecule to 2AP2 molecule. Where as in the case of GA-3AP compound, the theoretical bond lengths O16-C7 and O17-C7 are deviated by 0.038Å and 0.061Å respectively from XRD results is also due to proton transfer.

The knowledge of the Highest Occupied Molecular Orbital (HOMO) and Lowest Unoccupied Molecular Orbital (LUMO) levels of the molecules gives valuable information about their electronic properties, stability, and reactivity. The HOMO and LUMO orbitals signify the molecule's electron-donating and accepting abilities, respectively. HOMO and LUMO orbitals at the theoretical level for GA-2AP and GA-3AP molecules are illustrated in Fig. 14. HOMO is delocalized over the two gallic acid molecules and LUMO is delocalized over the one 2-aminopyridine molecule for 2:2 GA-2AP molecule while for 1:1 GA-3AP, both HOMO and LUMO are delocalized over almost complete molecule. The ionization energy, electron affinity and HOMO-LUMO energy gap are respectively, 6.0173eV, 1.7415eV and 4.2757eV for GA-2AP and 6.4733eV, 1.3002eV, 5.1732eV for GA-3AP. The chemical descriptors namely; Chemical potential, Global hardness, Global softness, and Electrophilicity index were also calculated and tabulated in the Table 8. Further, DFT study was also carried out for the starting compounds and compared with that of the noval repoted compounds. It was found that the energy gap of GA-2AP molecule is decreased by 0.5872 eV and that of GA-3AP molecules is incresed by 0.3103 eV when compared with the energy gap of the API, gallic acid. This shows that GA-2AP is more reactive and less stable than GA, whereas GA-3AP is less reactive and more stable than API GA. Because of this, the solubility of the API, GA will be more in GA-2AP form. Futher, when the energy gap values of the binary compounds were compared with that of the coformers, we found that, both the binary compounds are more reactive and less stable than the respective coformers.

Molecular Electrostatic Potential (MEP) map is a visual representation of the reactive sites in a molecule and is mapped with the colour scheme (electron rich regions are represented by red colour, while poor electron regions are represented by blue colour). MEP surface of the title

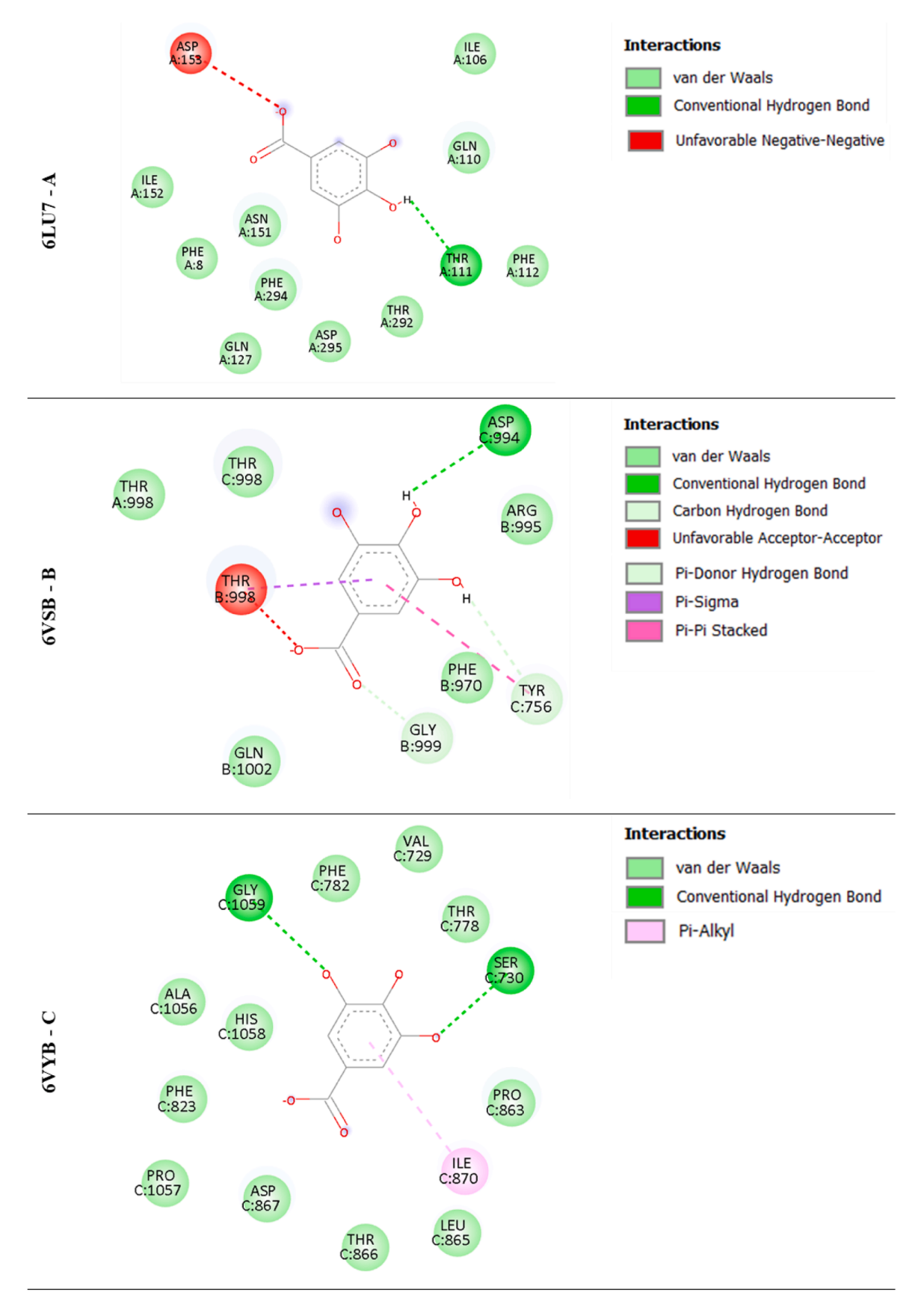


Fig. 18. 2D visualisation of the receptor-ligand interactions of GA-2AP.

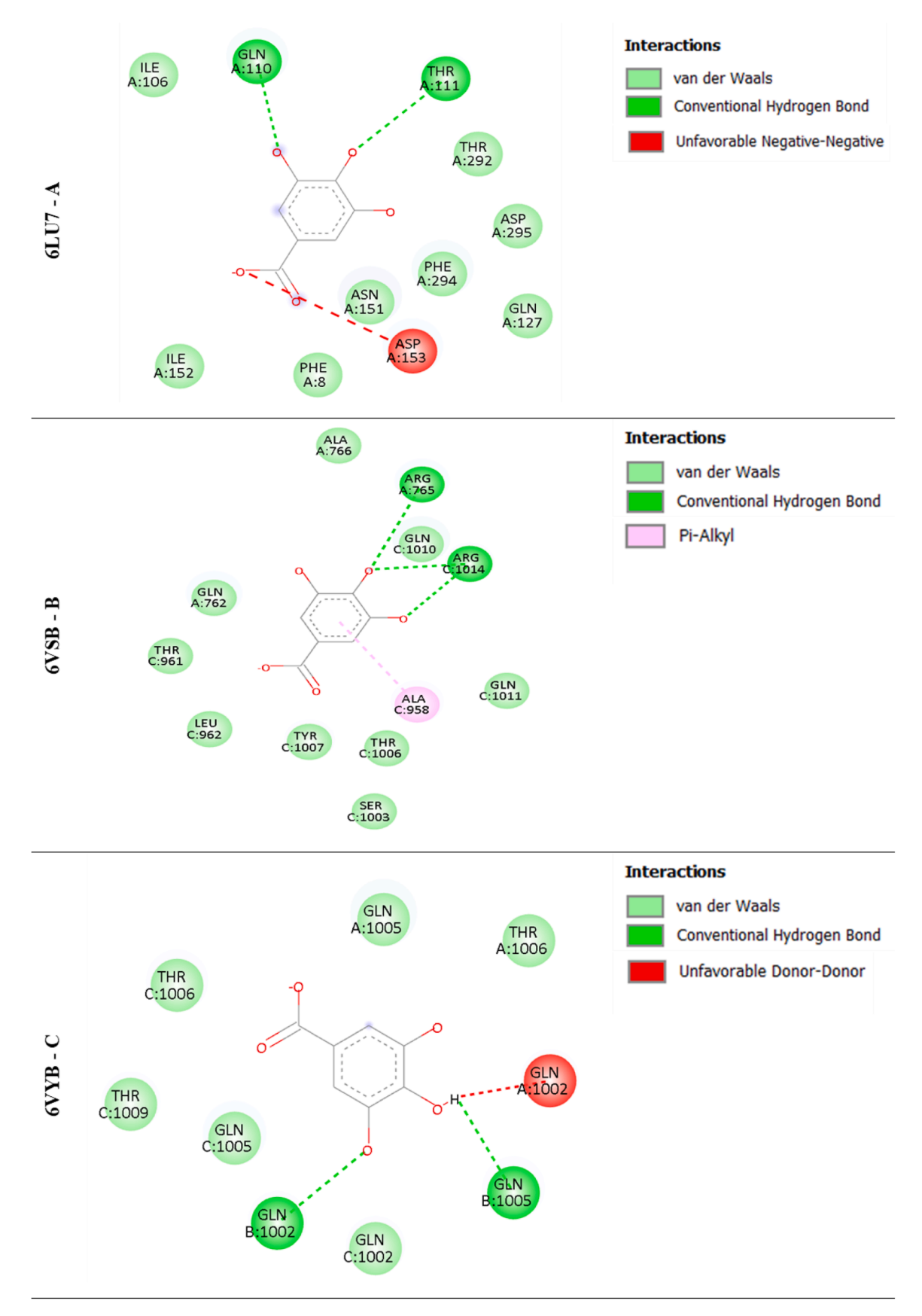


Fig. 19. 2D visualisation of the receptor-ligand interactions of GA-3AP.

compounds is shown in the Fig. 15. The MEP has the highest electronegative value of -0.0908 a. u. for GA-2AP and -0.09235 a. u. for GA-3AP, and they are highlighted by red colour (electrophilic reactive), indicating areas susceptible to attack by electron donors (nucleophiles). The high positive electrostatic potential has a value of +0.0908 a. u. for GA-2AP and +0.09235 a. u. for GA-3AP and indicated by the blue colour, signifies nucleophilic reactivity, highlighting potential sites for attack by electron acceptors (electrophiles). The electron rich/negative regions are mainly localized over C=O groups and over all the oxygen atoms of GA with red colour (which are most reactive sites for electrophilic attack), in both the compounds. Whereas, NH<sub>2</sub> groups and the hydrogen atoms of aminopyridine molecules are electron poor/positive regions with blue colour (which are most reactive sites for nucleophilic attack) [78].

#### 3.11. Molecular docking studies

In order to understand the molecular interactions between the synthesised compounds and the SARS-CoV-2, the docking of the compounds into the active sites of the selected targets was done. 6LU7 (A) is one of the key enzymes of the corona virus was chosen as a target protease [79, 80]. It is a potential therapeutic target for SARS-CoV-2 because of its critical function in mediating transcription and viral replication. The GA-2AP ligand binds in the substrate binding pocket and yields the binding score of -5.4 kcal/mol. The docking analysis shows one hydrogen bond interactions H2...THR111 of distance 2.146 Å. Unfavourable negative bond is formed between O5 and ASP153 with a distance of 4.04 Å. Van der waal's interactions are also present. While the GA-3AP ligand binds in the substrate pocket with a binding score of -5.4 kcal/mol. Two strong hydrogen bonds are present in the docking, of the type O15...GLN110 (1.99 Å) and O14...THR111 (2.2.88 Å). Here also unfavourable negative - negative interactions present between O15... ASP153.

It is thought that proteases and S- glycoproteins are an effective treatment approach for preventing the virus entry and its outbreak. Prefusion spike glycoprotein 6VSB (B) docked with the GA-2AP molecule gives binding score of -6.1 kcal/mol, while with GA-3AP give a score of -6.3 kcal/mol. In the case of GA-2AP, there exist a hydrogen bond interaction between H2.... ASP994 of the C protomer.  $\pi$ -  $\pi$  stacked interactions exist between the benzene ring and the TYR756 of the C protomer of distance 5.40 Å. Unfavourable acceptor- acceptor interaction exist between the THR998 of the A protomer and O5 (2.83 Å). Several hydrogen bond interactions are also observed. While for GA-3AP, three strong hydrogen bonds exist O14...ARG1014, O15... ARG1015 of C protomer and O14...ARG765 of A protomer. Pi-alkyl interactions persist between the benzene ring and the ALA958 of C protomer.

Due to the importance of S-protein in viral pathogenesis, it was one of the targeted proteins. Docking of GA-2AP with the targeted 6VYB (C) gives a binding score of -6.7 kcal/mol, while in the case of GA-3AP the bind score is found to be -6.5 kcal/mol. two hydrogen bond interactions are observed in the case of GA-2AP of the form O1...SER730 and O3... GLY1059 of the C protomer, both of distance near to 2 Å. Pi-alkyl interactions are also observed. In the case of GA-3AP, unfavourable donor-donor interactions are also observed of length 1.71 Å other than conventional hydrogen bond interactions. The best docking poses of the ligand with the targets showing the 3D and 2D visualisation of the receptor-ligand interactions are shown in Figs. 16, 17, 18 and 19.

#### 4. Conclusion

Two novel binary molecular salts of an API, gallic acid with 2 and 3 aminopyridines [GA-2AP and GA-3AP] taken in equimolar ratio were prepared by liquid assistant grinding method and crystalized using methanol solvent through slow evaporation method. The molecular salt formation of binary compounds was confirmed by the presence of

absorption band at 1326.67 cm<sup>-1</sup> for GA-2AP and at 1332.22 cm<sup>-1</sup> for GA-3AP corresponding to carboxylate anion (-COO-) through FTIR spectroscopy. Further this was confirmed in the single crystal X-ray structural analysis, which also revealed the stochiometric ratio as 2:2 and 1:1 respectively. Strong hydrogen bond interactions of the type O-H...O, N-H...O and relatively weak hydrogen bond interaction of the type C-H···O were contributed in the formation of the reported binary compounds. Expected highly stable supramolecular  $R_2^2(8)$  and  $R_1^2(5)$  ring synthons along with other ring frameworks were found in the crystal structures. Further, the structural analysis explored the significant  $\pi \cdots \pi$ interactions in packing the molecules of the binary molecular salt crystals along with the conventional hydrogen bond interactions. Further, thermal behaviour of the reported crystals was attributed through the major weight loss in TGA and the presence of sharp endothermic peak in DTA experiment has confirmed the melting point of GA-2AP and GA-3AP as 193°C and 213°C respectively. The intermolecular interactions were quantified through Hirshfeld surface analysis by generating 2D fingerprint plots which has revealed that H···H contacts are dominating in both the crystals. Further, 3D molecular surfaces were analysed to understand the role of interactions and enrichment ratio calculation revealed the significant contribution of O···H interaction in both crystals. The 3D energy framework analysis confirms the domination of electrostatic energy over dispersion and polarization energies. Further, DFT calculations evident that the GA-2AP with energy gap of 4.2757 eV may possess lesser stability, and better chemical reactivity compared to GA-3AP with energy gap of 5.1732 eV. Furthermore, DFT results were substantiated from the experimental UV-Vis spectroscopy. The docking analysis sheds light on the promising active interactions of the binary molecular salt crystals of gallic acid against Covid-19 main protease. The molecular salts well bind to the target protein sites of 6LU7 (A), 6VSB (B), and 6VYB (C) with the significant binding score of -5.4 kcal/mol and -5.4 kcal/mol, -6.1 kcal/mol and -6.3 kcal/mol, -6.7 kcal/mol and -6.5 kcal/mol for GA-2AP and GA-3AP respectively. Thus, our work offers an opportunity for the pharmaceutical industry to exploit the desired properties of gallic acid, which helps in expanding its medicinal applications. Furthermore, the biological screening of the reported compounds for drug design and applications could be the new avenue for the future research.

#### CRediT authorship contribution statement

K.L. Jyothi: Writing – original draft, Software, Resources, Methodology, Formal analysis, Data curation, Conceptualization. Karthik Kumara: Writing – original draft, Software, Formal analysis, Data curation. Viswanath M. Arya: Writing – original draft, Data curation. Vallabh S. Ghantasala: Writing – original draft, Software. T.N. Guru Row: Writing – review & editing, Supervision, Conceptualization. N.K. Lokanath: Writing – review & editing, Supervision.

#### Declaration of competing interest

The authors declare that they have no known competing financial interests or personal relationships that could have appeared to influence the work reported in this paper. We declare that, we have no conflict of interest in any direction for the manuscript.

#### Acknowledgments

The authors would like to thank the National Diffractometer Facility, Department of Studies in Physics, University of Mysore, Mysuru, and Solid State and Structural Chemistry Unit, Indian Institute of Science, Bengaluru for providing infrastructure and instrumentation facilities. Author, Dr. Karthik Kumara would like to thank BMS college of engineering, Bengaluru for the financial support under FRPS project no. R&D/FRPS/2022-23/PHY/03.

#### Appendix A. Supplementary data

CCDC Nos: 1906120 and 1902890 contains the supplementary crystallographic data of the synthesized compounds. These data can be obtained free of cost via <a href="http://www.ccdc.cam.ac.uk/conts/retrieving.html">http://www.ccdc.cam.ac.uk/conts/retrieving.html</a>, or from the Cambridge Crystallographic Data Centre, 12 Union Road, Cambridge CB2 1EZ, UK; fax: (+44) 1223–336–033; or e-mail: deposit@ccdc.cam.ac.uk

#### Supplementary materials

Supplementary material associated with this article can be found, in the online version, at doi:10.1016/j.molstruc.2025.144026.

#### Data availability

Data will be made available on request.

#### References

- [1] M. Singh, H. Barua, V.G.S. Jyothi, M.R. Dhondale, A.G. Nambiar, A.K. Agrawal, D. Kumar, Cocrystals by design: a rational coformer selection approach for tackling the API problems, Pharmaceutics 15 (4) (2023) 1161. https://www.mdpi. com/1999-4923/15/4/1161#.
- [2] A. Karagianni, M. Malamatari, K. Kachrimanis, Pharmaceutical cocrystals: New solid phase modification approaches for the formulation of APIs, Pharmaceutics 10 (1) (2018) 18. https://www.mdpi.com/1999-4923/10/1/18#.
- [3] N. Shan, M.J. Zaworotko, The role of cocrystals in pharmaceutical science, Drug Discov. Today 13 (9-10) (2008) 440–446, https://doi.org/10.1016/j. drudis.2008.03.004.
- [4] S.S. Bharate, Recent developments in pharmaceutical salts: FDA approvals from 2015 to 2019, Drug Discov Today 26 (2) (2021) 384–398, https://doi.org/ 10.1016/j.drudis.2020.11.016.
- [5] K. Sigfridsson, M.L. Ulvinge, L. Svensson, A.K. Granath, A case study where pharmaceutical salts were used to address the issue of low in vivo exposure, Drug Devel Ind. Pharm. 45 (2) (2019) 202–211, https://doi.org/10.1080/ 03639045.2018.1529184.
- [6] N.J. Babu, A. Nangia, Solubility advantage of amorphous drugs and pharmaceutical cocrystals, Cryst Growth Des. 11 (7) (2011) 2662–2679. https://pubs.acs.org/doi/abs/10.1021/cg200492w#.
- [7] N. Schultheiss, A. Newman, Pharmaceutical cocrystals and their physicochemical properties, Cryst Growth Des. 9 (6) (2009) 2950–2967. https://pubs.acs.org/doi/ full/10.1021/cg900129f.
- [8] K.L. Jyothi, R. Gautam, D. Swain, T.N. Guru Row, N.K. Lokanath, Cocrystals of gallic acid with urea and propionamide: supramolecular structures, Hirshfeld surface analysis, and DFT studies, Cryst Res Technol. 54 (8) (2019) 1900016, https://doi.org/10.1002/crat.201900016.
- [9] C.B. Aakeröy, D.J. Salmon, Building co-crystals with molecular sense and supramolecular sensibility, CrystEngComm 7 (2005) 439–448, https://doi.org/ 10.1030/b505883i
- [10] Mahesha K.L. Jyothi, N.K Lokanath, Understanding the formation of novel hydrated gallic acid-creatinine molecular salt: crystal structure, Hirshfeld surface and DFT studies, J. Chem. Crystallogr. 50 (2020) 410–421, https://link.springer. com/article/10.1007/s10870-019-00814-4.
- [11] G. Bolla, B. Sarma, A.K. Nangia, Crystal engineering of pharmaceutical cocrystals in the discovery and development of improved drugs, Chem Rev. 122 (13) (2022) 11514–11603. https://pubs.acs.org/doi/abs/10.1021/acs.chemrev.1c00987.
- [12] O.N. Kavanagh, D.M. Croker, G.M. Walker, M.J. Zaworotko, Pharmaceutical cocrystals: from serendipity to design to application, Drug Discov. Today 24 (3) (2019) 796–804, https://doi.org/10.1016/j.drudis.2018.11.023.
- [13] R. Samineni, J. Chimakurthy, S. Konidala, Emerging role of biopharmaceutical classification and biopharmaceutical drug disposition system in dosage form development: A systematic review, Turk J. Pharm. Sci. 19 (6) (2022) 706, https:// doi.org/10.4274/tjps.galenos.2021.73554.
- [14] K.L. Jyothi, K. Kumara, M.K. Hema, R. Gautam, T.G. Row, N.K. Lokanath, Structural elucidation, theoretical insights and thermal properties of three novel multicomponent molecular forms of gallic acid with hydroxypyridines, J. Mol. Struct. 1207 (2020) 127828, https://doi.org/10.1016/j.molstruc.2020.127828.
- [15] O.D. Putra, H. Uekusa, Pharmaceutical multicomponent crystals: Structure, design, and properties, Adv. Org. Cryst. Chem. Compr. Rev. (2020) 153–184. 2020, htt ps://link.springer.com/chapter/10.1007/978-981-15-5085-0\_9.
- [16] P. Sanphui, M.K. Mishra, U. Ramamurty, G.R. Desiraju, Tuning mechanical properties of pharmaceutical crystals with multicomponent crystals: voriconazole as a case study, Mol. Pharm. 12 (3) (2015) 889–897. https://pubs.acs.org/doi/abs/ 10.1021/mp500719t
- [17] N.A. Mir, R. Dubey, G.R. Desiraju, Strategy and methodology in the synthesis of multicomponent molecular solids: the quest for higher cocrystals, Acc Chem. Res. 52 (8) (2019) 2210–2220. https://pubs.acs.org/doi/abs/10.1021/acs.accounts .9b00211.

- [18] K. Jyothi, K. Kumara, V.S. Ghantasala, Crystal structure, supramolecular features, and antimicrobial properties of binary crystals of gallic acid and three isomers of hydroxypyridine, J. Mol. Struct. 1336 (2025) 142028, https://doi.org/10.1016/j. molstruc 2025 142028
- [19] N.U. Islam, M.N. Umar, E. Khan, F.A. Al-Joufi, S.N. Abed, M. Said, F.A. Khan, Levofloxacin cocrystal/salt with phthalimide and caffeic acid as promising solidstate approach to improve antimicrobial efficiency, Antibiotics 11 (6) (2022) 797, https://doi.org/10.3390/antibiotics11060797.
- [20] L. Padrela, E.G. de Azevedo, S.P. Velaga, Powder X-ray diffraction method for the quantification of cocrystals in the crystallization mixture, Drug Dev Ind Pharm 38 (8) (2012) 923–929. https://www.tandfonline.com/doi/abs/10.3109/036390 45 2011 633263
- [21] G.C. Zhang, H.L. Lin, S.Y. Lin, Thermal analysis and FTIR spectral curve-fitting investigation of formation mechanism and stability of indomethacin-saccharin cocrystals via solid-state grinding process, J. Pharm. Biomed. Anal. 66 (2012) 162–169, https://doi.org/10.1016/j.jpba.2012.03.039.
- [22] P.C. Vioglio, M.R. Chierotti, R. Gobetto, Pharmaceutical aspects of salt and cocrystal forms of APIs and characterization challenges, Adv. Drug. Deliv. Rev. 117 (2017) 86–110. https://www.sciencedirect.com/science/article/abs/pii/S0169409×17300984#preview-section-introduction.
- [23] E. Pindelska, A. Sokal, W. Kolodziejski, Pharmaceutical cocrystals, salts and polymorphs: Advanced characterization techniques, Adv Drug. Deliv. Rev. 117 (2017) 111–146, https://doi.org/10.1016/j.addr.2017.09.014.
- [24] J. Li, J. Sun, Application of X-ray diffraction and electron crystallography for solving complex structure problems, Acc Chem. Res. 50 (11) (2017) 2737–2745. https://pubs.acs.org/doi/abs/10.1021/acs.accounts.7b00366.
- [25] A. Mehta, R. Makhija, P. Barik, S. Dhiman, G. Das Gupta, V. Asati, Practical Perspectives and Roles of XRD in Drug Discovery: A Review, Curr. Anal. Chem 20 (7) (2024) 449–470, https://doi.org/10.2174/ 0115734110296435240323113938.
- [26] J.P. Zhang, P.Q. Liao, H.L. Zhou, R.B. Lin, X.M. Chen, Single-crystal X-ray diffraction studies on structural transformations of porous coordination polymers, Chem. Soc. Rev. 43 (16) (2014) 5789–5814. https://pubs.rsc.org/en/content/artic lelanding/2014/cs/c4cs00129j/unauth.
- [27] N. Nayeem, S.M.B. Asdaq, H. Salem, S. AHEl-Alfqy, Gallic acid: a promising lead molecule for drug development, J. Appl. Pharm. 8 (2) (2016) 1–4, https://doi.org/ 10.4172/1920-4159.1000213.
- [28] H.M. Chen, Y.C. Wu, Y.C. Chia, F.R. Chang, H.K. Hsu, Y.C. Hsieh, S.S. Yuan, Gallic acid, a major component of Toona sinensis leaf extracts, contains a ROS-mediated anti-cancer activity in human prostate cancer cells, Cancer Lett. 286 (2) (2009) 161–171, https://doi.org/10.1016/j.canlet.2009.05.040.
- [29] A. Borges, M.J. Saavedra, M. Simões, The activity of ferulic and gallic acids in biofilm prevention and control of pathogenic bacteria, Biofouling 28 (7) (2012) 755–767, https://doi.org/10.1080/08927014.2012.706751.
- [30] D.J. Seo, H.B. Lee, I.S. Kim, K.Y. Kim, R.D. Park, W.J. Jung, Antifungal activity of gallic acid purified from Terminalia nigrovenulosa bark against Fusarium solani, Microb pathog 56 (2013) 8–15, https://doi.org/10.1016/j.micpath.2013.01.001.
- [31] J.M. Kratz, C.R. Andrighetti-Fröhner, P.C. Leal, R.J. Nunes, R.A. Yunes, E. Trybala, C.M.O. Simões, Evaluation of anti-HSV-2 activity of gallic acid and pentyl gallate, Biol. Pharm. Bull. 31 (5) (2008) 903–907, https://doi.org/10.1248/bpb.31.903.
- [32] B.V. Kroes, A.J.J. Van den Berg, H.Q. Van Ufford, H. Van Dijk, R.P. Labadie, Anti-inflammatory activity of gallic acid, Planta Med. 58 (06) (1992) 499–504, https://doi.org/10.1055/s-2006-961535.
- [33] S. Sedehizadeh, M. Keogh, P. Maddison, The use of aminopyridines in neurological disorders, Clin neuropharmacol 35 (4) (2012) 191–200. https://journals.lww. com/clinicalneuropharm/abstract/2012/07000/the\_use\_of\_aminopyridines\_in\_n eurological.7.aspx.
- [34] M. Strupp, J. Teufel, A. Zwergal, R. Schniepp, K. Khodakhah, K. Feil, Aminopyridines for the treatment of neurologic disorders, Neurol. Clin. Pract. 7 (1) (2017) 65–76. https://journals.lww.com/clinicalneuropharm/abstract/2012/0 7000/the\_use\_of\_aminopyridines\_in\_neurological.7.aspx.
- [35] M. Strupp, J. Teufel, A. Zwergal, R. Schniepp, K. Khodakhah, K. Feil, Aminopyridines for the treatment of neurologic disorders, Neurol: Clin Pract 7 (1) (2017) 65–76, https://doi.org/10.1212/CPJ.000000000000321.
- [36] R.N. Rao, K. Chanda, 2-Aminopyridine–an unsung hero in drug discovery, Chem. Commun. 58 (3) (2022) 343–382. https://pubs.rsc.org/en/content/articlelandin g/2021/xx/d1cc04602k/unauth.
- [37] S. Hilton, S. Naud, J.J. Caldwell, K. Boxall, S. Burns, V.E. Anderson, I. Collins, Identification and characterisation of 2-aminopyridine inhibitors of checkpoint kinase 2, Bioorg. Med. Chem. 18 (2) (2010) 707–718, https://doi.org/10.1016/j. bmc.2009.11.058.
- [38] Z. Kibou, N. Aissaoui, I. Daoud, J.A. Seijas, M.P. Vázquez-Tato, N. Klouche Khelil, N. Choukchou-Braham, Efficient synthesis of 2-aminopyridine derivatives: Antibacterial activity assessment and molecular docking studies, Molecules 27 (11) (2022) 3439, https://doi.org/10.3390/molecules27113439.
- [39] R.A. Finch, M.C. Liu, A.H. Cory, J.G. Cory, A.C. Sartorelli, Triapine (3-aminopyridine-2-carboxaldehyde thiosemicarbazone; 3-AP): an inhibitor of ribonucleotide reductase with antineoplastic activity, Adv. Enzyme Regul. 39 (1) (1999) 3–12, https://doi.org/10.1016/S0065-2571(98)00017-X.
- [40] A. Baranyi, O. Fehér, Convulsive effects of 3-aminopyridine on cortical neurones, Electroencephalogr. Clin. Neurophysiol. 47 (6) (1979) 745–751, https://doi.org/ 10.1016/0013-4694(79)90303-1.
- [41] Z.G. Jiang, M.S. Lebowitz, H.A. Ghanbari, Neuroprotective Activity of 3-Amino-pyridine-2-Carboxaldehyde Thiosemicarbazone (PAN-811), a Cancer Therapeutic Agent, CNS Drug Rev 12 (1) (2006) 77–90, https://doi.org/10.1111/j.1527-3458.2006.00077.x.

- [42] S. Karki, T. Friščić, W. Jones, W.S. Motherwell, Screening for pharmaceutical cocrystal hydrates via neat and liquid-assisted grinding, Mol. Pharm. 4 (3) (2007) 347–354. https://pubs.acs.org/doi/abs/10.1021/mp0700054.
- [43] D. Hasa, G. Schneider Rauber, D. Voinovich, W. Jones, Cocrystal formation through mechanochemistry: from neat and liquid-assisted grinding to polymerassisted grinding, Angew Chem 127 (25) (2015) 7479–7483, https://doi.org/ 10.1002/cneg.201501638
- [44] D. Braga, L. Maini, F. Grepioni, Mechanochemical preparation of co-crystals, Chem. Soc. Rev. 42 (18) (2013) 7638–7648. https://pubs.rsc.org/en/content/artic lelanding/2013/cs/c3cs60014a/unauth.
- [45] A.S. Myerson, R. Ginde, Crystals, crystal growth, and nucleation. Handbook of industrial crystallization, Butterworth-Heinemann, 2002, pp. 33–65, https://doi. org/10.1016/B978-075067012-8/50004-5.
- [46] M.A. Yousef, V.R. Vangala, Pharmaceutical cocrystals: molecules, crystals, formulations, medicines, Cryst Growth Des. 19 (12) (2019) 7420–7438. htt ps://pubs.acs.org/doi/abs/10.1021/acs.cgd.8b01898.
- [47] S. Basavoju, D. Boström, S.P. Velaga, Pharmaceutical cocrystal and salts of norfloxacin, Cryst Growth. Des. 6 (12) (2006) 2699–2708. https://pubs.acs.org/ doi/abs/10.1021/ce060327x
- [48] Z. Rahman, C. Agarabi, A.S. Zidan, S.R. Khan, M.A. Khan, Physico-mechanical and stability evaluation of carbamazepine cocrystal with nicotinamide, Aaps Pharmscitech. 12 (2011) 693–704. https://link.springer.com/article/10.120 8/s12249-011-9603-4.
- [49] A. Kiguchiya, R. Teraoka, T. Sakane, E. Yonemochi, A new method for classification of salts and cocrystals using solid-state UV spectrophotometry, Chem. Pharm Bull. 67 (9) (2019) 945–952, https://doi.org/10.1248/cpb.c18-00743.
- [50] J. Quertinmont, T. Leyssens, J. Wouters, B. Champagne, Unraveling the Effects of Co-Crystallization on the UV/Vis Absorption Spectra of an N-Salicylideneaniline Derivative. A Computational RI-CC2 Investigation, Molecules 25 (19) (2020) 4512, https://doi.org/10.3390/molecules25194512.
- [51] S.P Bruker, 1999;(b) AL Spek, Acta Crystallogr. D: Biol. Crystallogr. 65 (2009) 148–155.
- [52] G.M. Sheldrick, Phase annealing in SHELX-90: direct methods for larger structures, Acta Crystallogr. A: Found Crystallogr. 46 (6) (1990) 467–473, https://doi.org/ 10.1107/S0108767390000277
- [53] G.M. Sheldrick, T.R. Schneider, [16]SHELXL: High-resolution refinement, in: Methods in enzymology, 277, Elsevier, 1997, pp. 319–343, https://doi.org/ 10.1016/S0076-6879(97)77018-6.
- [54] A. Spek, Single-crystal structure validation with the program PLATON, J. Appl. Crystallogr. 36 (1) (2003) 7–13.
- [55] C.F. Macrae, P.R. Edgington, P. McCabe, E. Pidcock, G.P. Shields, R. Taylor, M. Towler, J. Streek, Mercury: visualization and analysis of crystal structures, J appl crystallogr 39 (3) (2006) 453–457.
- [56] A. Sarkar, S. Rohani, Cocrystals of acyclovir with promising physicochemical properties, J. Pharm. Sci. 104 (1) (2015) 98–105, https://doi.org/10.1002/ ins. 24248
- [57] L.T. Ferreira, R.T. Alarcon, G.L. Perpétuo, G. Bannach, Investigation and characterization by TG/DTG–DTA and DSC of the fusion of Riboflavin, and its interaction with the antibiotic norfloxacin in the screening of cocrystal, J. Therm. Anal. Calorim. 136 (2) (2019) 581–588. https://link.springer.com/article/10.100 7/s10973-018-7696-7.
- [58] L. Pan, F. Dai, G. Li, S. Liu, A TGA/DTA-MS investigation to the influence of process conditions on the pyrolysis of Jimsar oil shale, Energy 86 (2015) 749–757, https://doi.org/10.1016/j.energy.2015.04.081.
- [59] M.A. Spackman, J.J. McKinnon, Fingerprinting intermolecular interactions in molecular crystals, CrystEngComm 4 (66) (2002) 378–392, https://doi.org/ 10.1039/B203191B.
- [60] S.K. Wolff, D.J. Grimwood, J.J. McKinnon, M.J. Turner, D. Jayatilaka, M. A. Spackman, CrystalExplorer (Version 3.1), Univ. West Aust. (2012). http://crystalexplorer.sch.uwa.edu.au/.
- [61] J.J. McKinnon, D. Jayatilaka, M.A. Spackman, Towards quantitative analysis of intermolecular interactions with Hirshfeld surfaces, Chem. Commun. (37) (2007) 3814–3816, https://doi.org/10.1039/B704980C.
- [62] K. Kumara, M. Jyothi, N. Shivalingegowda, S.A. Khanum, L.N. Krishnappagowda, Synthesis, characterization, crystal structure and Hirshfeld surface analysis of 1-(4-

- ethoxyphenyl)-3-(4-methylphenyl) prop-2en-1-one, Chem. Data Collect 9 (2017) 152–163, https://doi.org/10.1016/j.cdc.2017.06.003.
- [63] P.R. Spackman, M.J. Turner, J.J. McKinnon, S.K. Wolff, D.J. Grimwood, D. Jayatilaka, M.A. Spackman, CrystalExplorer: A program for Hirshfeld surface analysis, visualization and quantitative analysis of molecular crystals, J. Appl. Crystallogr. 54 (3) (2021) 1006–1011.
- [64] K.L. Jyothi, M.K. Hema, K. Kumara, T.N. Guru Row, N.K. Lokanath, Structural elucidation of 1:4:4 stochiometric form of thymine gallic acid cocrystal hydrate: Hirshfeld surface analysis, 3D energy framework, DFT calculations, and SARS CoV-2 docking studies, J. Mol. Struct. 1280 (2023) 135072, https://doi.org/10.1016/j.molstruc.2023.135072.
- [65] P. Hohenberg, W. Kohn, Inhomogeneous electron gas, Phys. Rev. 136 (3B) (1964) B864, https://doi.org/10.1103/PhysRev.136.B864.
- [66] W. Kohn, L.J. Sham, Self-consistent equations including exchange and correlation effects, Phys. Rev. 140 (4A) (1965) A1133, https://doi.org/10.1103/PhysRev.140. A1133
- [67] Frisch, M.; Trucks, G.; Schlegel, H.; Scuseria, G.; Robb, M.; Cheeseman, J.; Scalmani, G.; Barone, V.; Petersson, G.; Nakatsuji, H., Gaussian–16 Revision C. 01, 2019. Gaussian Inc., Wallingford CT Search PubMed.
- [68] T. Koopmans, Über die Zuordnung von Wellenfunktionen und Eigenwertenzu den einzelnenElektroneneines Atoms, Physica 1 (1-6) (1934) 104–113.
- [69] M. Robb, New Chemistry with Gaussian 16 & GaussView 6, Expand Limits Comput. Chem. (2022) ht tps://gaussian.com/g16new.
- [70] K. Kumara, M. Jyothi, S. Kouser, A.H.U. Kumar, I. Warad, S.A. Khanum, N. K. Lokanath, Structural investigations and theoretical insights of a polymethoxy chalcone derivative: Synthesis, crystal structure, 3D energy frameworks and SARS CoV-2 docking studies, J. Mol. Struct. 1272 (2023) 134226, https://doi.org/10.1016/j.molstruc.2022.134226.
- [71] P. Bansal, R. Kumar, J. Singh, S. Dhanda, In silico molecular docking of SARS-CoV-2 surface proteins with microbial non-ribosomal peptides: identification of potential drugs, J. Proteins Proteom. 12 (2021) 177–184, https://doi.org/ 10.1007/s42485-021-00072-z.
- [72] A. Subbaiyan, K. Ravichandran, S.V. Singh, M. Sankar, P. Thomas, K. Dhama, Y. S. Malik, R.K. Singh, P. Chaudhuri, In silico Molecular Docking Analysis Targeting SARS-CoV-2 Spike Protein and Selected Herbal Constituents, J. Pure Appl. Microbiol. 14 (2020) 989–998, https://doi.org/10.22207/JPAM.14.SPL1.37.
- [73] O. Trott, A.J. Olson, AutoDock Vina: Improving the speed and accuracy of docking with a new scoring function, efficient optimization, and multithreading, J. Comput. Chem. 31 (2010) 455–461, https://doi.org/10.1002/jcc.21334.
- [74] D. Studio, Discovery studio, Accelrys (2008), 2.1.
- [75] A. Kamal, J.R. Tamboli, M.J. Ramaiah, S.F. Adil, G. Koteswara Rao, A. Viswanath, M. Pal-Bhadra, Anthranilamide–Pyrazolo [1, 5-a] pyrimidine Conjugates as p53 Activators in Cervical Cancer Cells, ChemMedChem 7 (8) (2012) 1453–1464, https://doi.org/10.1002/cmdc.201200205.
- [76] M. Bán, P. Bombicz, J. Madarász, Thermal stability and structure of a new cocrystal of theophylline formed with phthalic acid: TG/DTA-EGA-MS and TG-EGA-FTIR study, J. Therm Anal. Calorim. 95 (3) (2009) 895–901, https://doi.org/ 10.1007/s10973-007-8902-1
- [77] C.F. Mackenzie, P.R. Spackman, D. Jayatilaka, M.A. Spackman, CrystalExplorer model energies and energy frameworks: extension to metal coordination compounds, organic salts, solvates and open-shell systems, IUCrJ 4 (5) (2017) 575–587, https://doi.org/10.1107/S205225251700848X.
- [78] C. Jelsch, K. Ejsmont, L. Huder, The enrichment ratio of atomic contacts in crystals, an indicator derived from the Hirshfeld surface analysis, IUCrJ 1 (2014) 119–128, https://doi.org/10.1107/S2052252514003327.
- [79] T.C. Raveesha, M.K. Hema, K.J. Pampa, P.G. Chandrashekara, K. Mantelingu, T. Demappa, N.K. Lokanath, Analysis of supramolecular self-assembly of two chromene derivatives: Synthesis, crystal structure, Hirshfeld surface, quantum computational and molecular docking studies, J. Mol. Struct. 1225 (2021) 129104, https://doi.org/10.1016/j.molstruc.2020.129104.
- [80] K.L. Jyothi, M.K. Hema, K. Kumara, N.K. Lokanath, Gallic acid-butyramide monohydrate cocrystal: Crystal growth, Structural insights, Theoretical calculations and Molecular docking studies against COVID-19 main protease, Curr. Chem. Lett. 12 (2023) 235–248, https://doi.org/10.5267/j.ccl.2022.6.004.